

ABSTRACT

HINTON, CORY DIONIS. Investigation of Stability in an Electrostatically Actuated Film. (Under the direction of Dr. Thomas Ward.)

An argument for employing dimensional analysis to explore stability in an electrostatically actuated flexible electrode is presented. The electrode is configured as a cantilever beam, as many applications in MEMs, medical devices, and sensing devices have been studied for years. This study investigates a macro scale beam (length = 100mm - 150mm), for applications in cooling fan and flapping micro air vehicle devices. The influence of scale is validated, voltage potential and frequency contributions are quantitatively analyzed, and a comparison of input signal (analog versus digital) is discussed. Based on experimental data and numerical models, characteristics of stability are analyzed for conclusions on design principles at the macro-scale. Experimental results for damping also validate numerical model constraints. Results from phase plots suggest that stability not only exists for a linear (triangular) input signal, but the range of stability is wider than that of a sinusoidal signal with losses in amplitude of oscillation. The results presented could influence design considerations and processes for various micro- and macro-scale devices.

© Copyright 2013 by Cory Dionis Hinton

All Rights Reserved

Investigation of Stability in an Electrostatically Actuated Film

by
Cory Dionis Hinton

A thesis submitted to the Graduate Faculty of
North Carolina State University
in partial fulfillment of the
requirements for the degree of
Master of Science

Mechanical Engineering

Raleigh, North Carolina

2013

APPROVED BY:

Dr. Robert Nagel

Dr. Lawrence Silverberg

Dr. Thomas Ward
Chair of Advisory Committee

DEDICATION

I dedicate this work to Danna, my love, and my family and friends who supported me with laughter, money, good times, food, and love as I walked this road of lengthy, rough terrain.

BIOGRAPHY

Cory Dionis Hinton was born in Savannah, Georgia on September 13, 1988. Born into a military family Cory was reared from an early age to appreciate hard work and achievement. Having lived very many places while still in his formative years, Cory began developing a sense of the greatness of the world around him. First taking to musical instruments, Cory built a passion for music, and working with his hands, and after much of the time spent in grade school was met with year after year of concert bands, marching bands, jazz bands and the like, Cory decided that he wanted to attend a university where he could meld his passion for music and his delight in working with his hands. North Carolina State University was his first choice and he enjoyed studying at this institution so much that he continued on his academic career from an undergraduate to graduate studies. Upon finishing his master level studies, Cory intends to marry his best friend, lover and sister in Christ, Danna Marie to begin a happy life together. He later plans to pursue a PhD and teach students, not just about his areas of expertise, but about life and truth.

ACKNOWLEDGEMENTS

I would like to thank Dr. Thomas Ward for his support and encouragement in pursuing this project topic for a thesis, from which I have not only learned much of concerning the subject matter but also a great deal about academia. I would also like to thank Dr. Nagel who has been a great mentor and supporter of my graduate studies since I met him as a senior in my undergraduate career. The coaching and encouragement from Dr. Nagel has been a guide for my studies as a graduate student, and for his help I am forever grateful. I would like to thank Dr. Silverberg for his encouragement and for serving on my committee he is a man whose intelligence I have always admired. I would also like to thank the faculty and staff members who I have come to know, who always encouraged me to push on and keep looking towards the goal.

TABLE OF CONTENTS

LIST OF TABLES	vii
LIST OF FIGURES	viii
Chapter 1 Introduction	1
1.1 Literature Review	3
1.2 Problem Motivation & Background Theory	5
1.3 Numerical Model	11
Chapter 2 Experiments	14
2.1 The Setup	14
2.2 Procedure	16
2.3 Experimental Analysis Technique	17
2.4 Numerical Analysis	18
Chapter 3 Results from Image Analysis	21
3.1 Influence of Voltage	22
3.2 Influence of Frequency	23
3.3 Influence of Scale	26
3.3.1 Sinusoidal Signal Data Set	27
3.3.2 Triangular Signal Data Set	30
3.4 Numerical Model Results	31
Chapter 4 Discussion	33
4.1 Frequency Density	33
4.2 Phase Plots	36
Chapter 5 Error Analysis	41
Chapter 6 Conclusions	42
REFERENCES	45
APPENDICES	47
Appendix A Non-dimensionalization of the Euler-Bernoulli Beam Equation	48
A.1 Non-dimensional Analysis	48
Appendix B MATLAB Code	51
B.1 Data Extraction from Videos	51
Appendix C MATLAB Code	55
C.1 Data Analysis	55
C.2 Phase Mapping	57

Appendix D Code	59
D.1 Fourth-order Runge-Kutta Model of Non-dimensionalized Beam	59

LIST OF TABLES

Table 2.1	Table of parameters	15
-----------	-------------------------------	----

LIST OF FIGURES

Figure 1.1	Large force electrostatic comb drive (Image courtesy:www.memx.com) . .	2
Figure 1.2	Three-gram dragonfly (Image courtesy:www.sciencedaily.com)	3
Figure 1.3	Humming bird bio signal for wing beat (Altshuler et al, Neurimascular control of wingbeat kinematics in Anna’s hummingbirds, 2010)	6
Figure 1.4	Diagram of the flexible cantilevered film noting important parameters. . .	8
Figure 2.1	Schematic of experimental setup and region of interest used in the analysis	15
Figure 2.2	Input signals for electrostatic actuation, the first being a sine wave (left) and the second being a triangle wave (right).	17
Figure 2.3	Underdamped oscillation of the film used to determine viscous damping coefficient.	18
Figure 2.4	Logarithmic curve fit used to determine damping coefficient.	19
Figure 3.1	Position VS time of the film tip for various voltages (4 Hz, 0-10kV, sinusoidal signal, 13mm X 150mm X 0.2mm).	22
Figure 3.2	Graphical explanation of phase locking for a sinusoidal input signal. . . .	24
Figure 3.3	Graphical explanation of phase locking for a triangular input signal. . . .	24
Figure 3.4	Position versus time for the non-linear input:	25
Figure 3.5	Position versus time for the linear input: 3Hz (7kV, 13mm x 100mm, 0.2mm).	26
Figure 3.6	FFT plot for 13mm x 150mm x 0.2mm beam at 4Hz and 10kV.	27
Figure 3.7	Frequency output versus voltage for beam sizes	29
Figure 3.8	Position versus time data for the 13mm X 100mm X 0.2mm specimen at 2Hz and 7kV.	31
Figure 3.9	Influence of frequency in numerical model for the 13mm X 100mm X 0.2mm specimen at 7Hz and 7kV.	32
Figure 4.1	Frequency density plots for the 13mm x 150mm x 0.2mm film specimen.	34
Figure 4.2	Phase plot graphs for a simple oscillator (left), sinusoidal signal (center),	37
Figure 4.3	Phase plot graphs for the numerical model sinusoidal signal	39

Chapter 1

Introduction

Electrostatic actuation is a process by which a build-up of charge produces an electric field and, as result, attractive forces are established between two electrodes one of which is allowed to move. This process by which charge build up produces capacitance and by energy relations in turn produces an electric field between electrodes is founded and thoroughly explained in electrostatics theory[1, 2]. Relating the motion of the *mover* of the electrostatic device to the capacitive interactions of the *mover* and the *stator*, expressions for motion of the *mover*, static or dynamic, are developed. These guiding principles have fueled interest in studying characteristics of motion in such actuators from many years past to now. Electrostatically actuated devices find use in various fields of study and application. For years, micro-electromechanical (MEM) devices have employed both cantilever and fixed-end micro beams, usually of polymer substrate, in applications of sensors/detection devices, medical devices and even transducers in biomechanical sensors[3]. Most literature on this topic focuses only in the micro-cantilever realm. However, for use in novel fanning devices, the wing structure of flapping micro air vehicles (MAVs), as well as the pressure wave source for electrostatic loud speakers, the need for greater study of macro scale beams in various environments is apparent. Fig. 1.1 depicts a common electrostatic MEMs device and in Fig. 1.2 is a novel machine highlighting the potential for MAV drone technology.

Flexible conducting materials may present a viable continuum structure for such devices

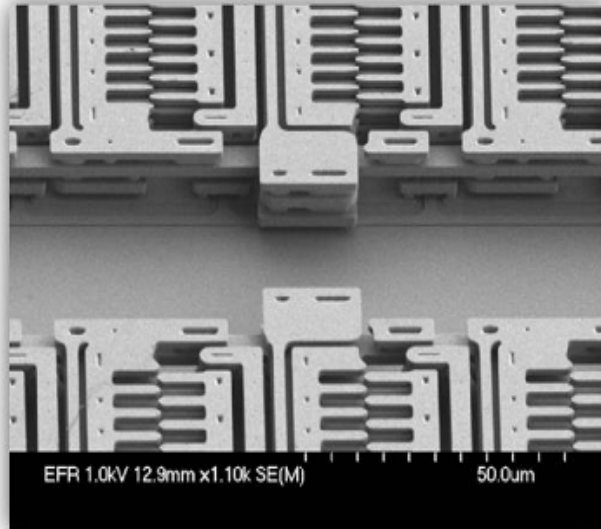


Figure 1.1: Large force electrostatic comb drive (Image courtesy:www.memx.com)

as seen in the wing film of the three-gram dragonfly of Fig. 1.2. Because there are a number of design considerations when implementing such a material in the various devices mentioned, due concern is needed in the context of static and dynamic motion studies and various other areas of interest. A number of deflection models, experimental parameter influence analysis and comparison would prove useful in producing a sufficiently applicable device. This study makes conclusions concerning the stability of electrostatic actuation of a flexible conducting material. While this is a topic of discussion for micro-sized bio-sensors and engines (such as the comb drive of Fig. 1.1), conversation on the macro-scale could prove particularly interesting and applicable as well. Useful conclusions from this research could bolster advances in technological development of MEMs and macro scale devices for use in biomedical, aerospace and other fields.



Figure 1.2: Three-gram dragonfly (Image courtesy:www.sciencedaily.com)

1.1 Literature Review

As noted, study of electrostatically actuated continuum structures has in years past been limited to micro-scale structures in devices for use in biomedical and electromechanical sensors and actuators where special attention is needed in design optimization of such mechanisms. Driven by demands for innovation in electronic devices and integration of conducting plastics therein, much of the research conducted in the micro-scale (with deflections and displacements in the nano-scale) considers use for close-proximity sensing or actuation with considerably low voltages noting the need to avoid pull-in instabilities[4]. Such instabilities result in over-extension of the electrostatic structure or in worse cases reduction of the gap distance to zero. In these studies, researchers have paid particular attention to the need for multi-physics when addressing the dynamics of such structures, mainly due to the various levels of coupling, such as fluid dynamic and inertial, that takes place with these microstructures[5]. Of specific interest for electrostatic

actuation is the micro-beam structure that has also been studied for its bending characteristics as presented in Ref.[6]; here the importance of experimental validation is stressed and inclusion of non-linearity terms in modeling. Such structures are found in various device applications today, however implementation of conductive continuum structures on the macro-scale is of unique interest for research today.

When performing motion observations and dynamic studies of electrostatically actuated flexible conducting plastics, most select DC switching and sinusoidal variation of charge build-up as the cyclic forcing[7, 8]. Special attention given to these signal types is specific for the applications in which the structures are implemented; however consideration of more signal types will give useful insight into the influencing factors of dynamic response opening new areas of study for signal usage in special applications. Researchers also address the need to consider the influence of damping effects due to various fluidic environments. Ref.[9] explains the need to characterize the damping coefficient by the quality factor and compare results to previous work on the subject. Further care is taken in Ref.[3] to address the need to further consider the effects of damping in situations of immersion in mediums of higher viscosity modeling the viscous damping coefficient using an Euler-Bernoulli beam equation based model and a damped harmonic oscillator model as well as explaining the relationship of mass shift due to frequency shift. Limiting factors such as maximum frequency and critical gap distance are of great importance when modeling the beam structure for design purposes. Special care in mathematical description and modeling analysis when the micro beam length extends into the milli-meter scale because the effects of gravity become more influential[10] noting that the instabilities due to pull-in occur at lower voltages.

Due to size constraints in design of MEMs actuators and sensors, most do not consider a second-phase material for improved conductivity, but rely on the conductivity of organic or silicon-based substrates for experimental studies[6, 9]. This is useful for ease of manufacturability via bulk micromachining. In considering second-phase materials in addition to doping strategies, a good study of macro-scale beams is introduced in that comparing elasticity prop-

erties and conductivity could relate to stability. Stability has been a topic of various studies for reasons of safe and reliable entry into sensors and actuators in the various applications mentioned[11, 12]. Rochus et al.[11] discusses the instability that occurs due to pull-in for the dynamic case, and note that the mere coupling of electrostatics to continuum mechanics gives rise to instabilities. These instabilities are studied with phase plots and frequency sweeps. Those in Ref. [12] note that instabilities often occur when the frequency of the forcing and the natural frequency are not matched. An appreciable range of stability occurs near the natural frequency and its harmonics, but this is also influenced by the voltage. Necessary peering into the signal influence, voltage, and frequency is essential for understanding the dynamical behavior of flexible films as their use expands to the macro-scale.

1.2 Problem Motivation & Background Theory

Particularly considering the design of flapping MAVs, properties and dynamics of the wing structure is of great interest for biomimetic drone technology. It is important to note that specific care is needed when placing drone technology in compromising environments (where virulent air currents, transient wind gusts, etc. are present). Many biologists and animal scientists have studied the bio-signal control relation to wing dynamics of small birds and insects, noting in their research the pivotal stroke and flexion of insect wings both contribute to locomotion (and coincidentally the need for control) in water and air[13]. One such study employed electromyogram recordings to observe and understand the muscle activation of hummingbirds when challenged to hover in various low-density environments finding that the hummingbird bio-signal does in fact modulate in different patterns for the various scenarios[14]. Fig. 1.3 depicts one such bio-signal. Others yet have quantified the influence of inertial bending over fluid dynamic interactions on the wing[15], concluding that elastic properties outweigh fluid-dynamic environmental considerations in flexible wing design. However, studies note the limitations of modeling a flexible appendage as a simple linear beam when density or the fluid medium af-

ffects the fluid-solid coupling such that it is of concern for model accuracy. Studies also note the importance of wing shape interactions with fluid dynamic forces, and the effectiveness of computational modeling for flexible wing design[16, 17]. It is also important to note the need to emulate animal and insect wings with proper materials that are common the design engineers needs. For conductivity, elastic properties, etc. the material of a cantilever beam the will mimic a wing is essential.

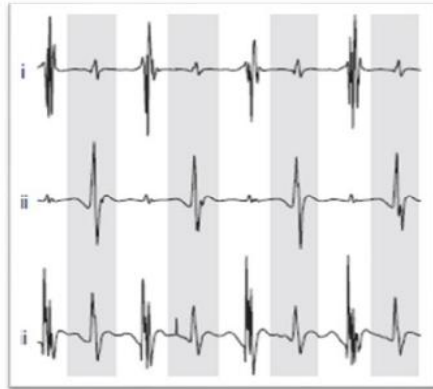


Figure 1.3: Humming bird bio signal for wing beat (Altshuler et al, Neurimascular control of wingbeat kinematics in Anna’s hummingbirds, 2010)

Indium oxide (In_2O_3), a ceramic particulate composite, is commonly used in applications requiring significant electrical conductivity. The indium oxide component is generally complemented with polyethylene-terephthalate (PET) due to its inherent electrical properties. Industries take advantage of the flexibility of the PET, the matrix of this composite, and the high conductivity of the indium oxide (the second-phase material). Specific basic and applied research applications require the indium oxide be combined, or doped with other particulate materials such as zinc, tin, gold, silver, and others achieving various electrical, mechanical and

chemical properties.

In this study, an indium oxide based electrode is configured as a cantilever beam and via an electrical circuit is dynamically actuated by an electric field between the flexible beam electrode and a stationary ground electrode. The resulting motion is defined and analyzed for influences of geometric scale, frequency and voltage. From these aspects, in addition to comparing sinusoidal (non-linear) and triangular (piecewise linear) signal inputs of the applied electric field, stability characteristics using phase plots and fast-fourier transform (FFT) data is discussed. To provide useful design practice tools, a numerical model is validated with experimental results.

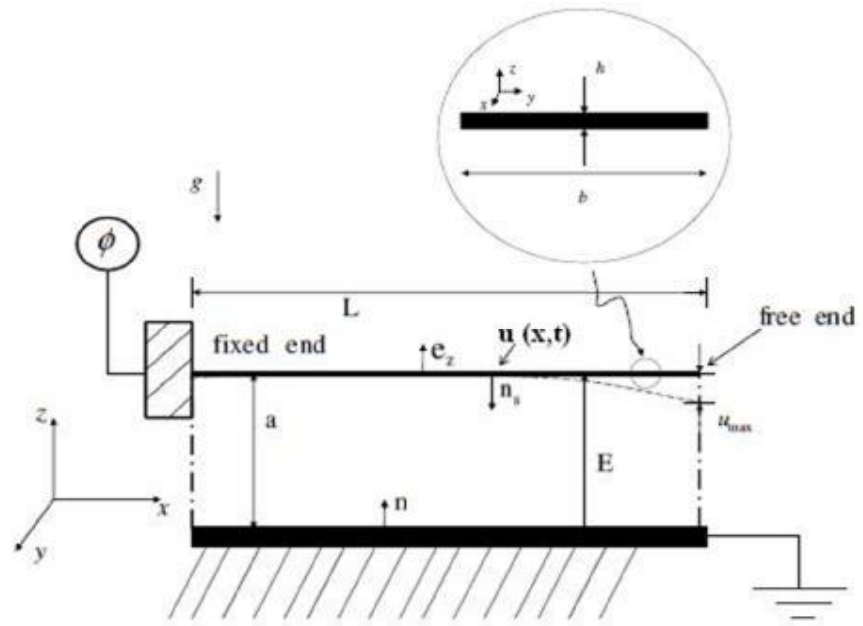


Figure 1.4: Diagram of the flexible cantilevered film noting important parameters.

Euler-Bernoulli beam theory is the basis of the mechanical deflection analysis. Assuming, as in classical beam theory, that the end of the beam remains perpendicular to the centerline, higher order terms of deflection can be neglected. This is a very useful assumption as the physical intuitiveness is lost in the higher order terms. To further simplify the model, the deflections of the beam are assumed to be small in comparison to the length of the beam this is an essential and acceptable assumption considering the voltage levels applied in actuation do not deflect the beam more than some millimeters, whereas the length of the beam is on a decimeter scale. Linear strain is also assumed to confine the deflection to the directions normal to the beam faces.

Accounting for the linear density (mass per unit length) ρ , cross-sectional area A , elastic modulus E , area moment of inertia I , the equation for the beam is then

$$\rho A \frac{\partial^2 u}{\partial t^2} = -EI \frac{\partial^4 u}{\partial x^4} + \sum F_{ext} \quad (1.1)$$

where $u(x, t)$, the modal deflection of the beam is a function of position along the beam x and time t , and F_{ext} represents any forces applied to the beam system by sources in the environment of the flexible beam.

Because no electrons are passed through the two electrodes, mainly due to the assumption that air is a poor conductor of electricity (i.e. an insulator), and charge tends to build on the faces of the electrodes, electrostatic theory applies. To simplify the expression for an electrostatic actuation force, the electrodes are assumed to remain parallel during the dynamic actuation of the flexible electrode. The electric field is assumed to have uniform distribution over the face of the stator electrode (grounded), so as to exclude any spatial variation from the electrostatic force.

Thus, the electric field has the form

$$E_{es} = -e_z \frac{\partial \phi}{\partial z} \quad (1.2)$$

where ϕ represents the electric potential, or voltage, and e_z is the unit normal on the top face of the flexible electrode (oriented positively upward).

Maxwells stress tensor is a common relation between the structural mechanics and electrostatics of a beam that responds to attractive and/or repulsive electric fields.

Maxwells tensor for electrostatic force in 3-dimensional space is

$$F_e = \int \int_S T_{ij} dA_{face} \quad (1.3)$$

Looking into the electrostatic field tensor:

$$T_{ij} = \epsilon_o \left(E_{es,i} E_{es,j} - \frac{1}{2} \delta_{ij} E_{es}^2 \right) \quad (1.4)$$

where $i=1, 2, 3$, and $j = 1, 2, 3$. Indices 1, 2 and 3 correspond to the x, y and z directions, respectively.

Using an energy analogy to relate the capacitance, electric field and voltage, the force on the flexible electrode that follows from Eq. 1.3 and Eq. 1.4 is then simplified to:

$$F_e = \frac{\phi^2(t) b \epsilon_r \epsilon_o}{a^2 L} \quad (1.5)$$

Here ϵ_0 and ϵ_r represent the permittivity of free-space and the relative permittivity respectively. Also represented are the electrode sparation, or gap distance (assumed constant, for simplicity), a , beam width, b , and length of the beam, L , as illustrated in Fig. 1.4. Note that this force becomes nonlinear when the forcing is sinusoidal due to AC voltage input, $\phi(t)$. The signal input for the electrostatic force is tested for two wave forms in this study. The first is a sinusoidal input wave that is described by

$$\phi(t) = \phi_1 + \phi_2 \sin \omega_i t$$

where ϕ_1 represents the electric DC potential and ϕ_2 represents the AC component of the elec-

tric potential signal input.

(Note: $\phi_1 = \phi_2$). This then simplifies to

$$\phi(t) = \phi_1 (1 + \sin \omega_i t) \quad (1.6)$$

The second is a symmetric triangle wave form as described by

$$\phi(t) = - \left| t - \frac{1}{4\omega_i} \right| + 2\phi_1 \quad (1.7)$$

$$\phi = \phi \left(t + \frac{1}{\omega_i} \right)$$

Other external forces on the beam include gravitational and damping forces which are modeled mathematically by the following equations:

$$F_g = \rho A g \quad (1.8)$$

$$F_d = \frac{c}{L} \frac{\partial u}{\partial t} \quad (1.9)$$

where g is the acceleration due to gravity and c is the damping coefficient. Accounting for distributive interaction with the beam continuum structure, these forces are assumed to be constant and proportional to velocity, respectively, over the entire beam.

Substituting Eq. 1.5, Eq. 1.8 and Eq. 1.9 into Eq. 1.1, the equation of motion for the electrostatically actuated beam is

$$\rho A \frac{\partial^2 u}{\partial t^2} = -EI \frac{\partial^4 u}{\partial x^4} - \frac{c}{L} \frac{\partial u}{\partial t} - \rho A g + \frac{\phi^2(t) b \epsilon_r \epsilon_o}{a^2 L} \quad (1.10)$$

1.3 Numerical Model

Taking the approach of dimensional analysis, the Euler-Bernoulli formulation with external forces is non-dimensionalized and analyzed via a fourth-order Runge-Kutta model (See Ap-

pendix D for MATLAB script). Approximations are based on the before mentioned assumptions and constraints. Non-dimensionalization of the equation of motion (Eq. 1.9) is as follows:

$$\frac{\partial^2 u^*}{\partial t^{*2}} = -\frac{\partial^4 u^*}{\partial x^{*4}} - \frac{c}{\omega \rho AL} \frac{\partial u^*}{\partial t^*} - \frac{g}{\omega^2 L} + \frac{\phi^2(t) b \epsilon_r \epsilon_o}{a^2 \omega^2 \rho AL^2} \quad (1.11)$$

where the bending deflection of the beam in time and space is non-dimensionalized by the length of the beam, $u^* = \frac{u}{L}$ as are the velocity and acceleration. The time variable used to compute partial derivatives of the bending deflection is non-dimensionalized by a frequency in terms of radians per second, $t^* = \omega t$, and the position along the beam is non-dimensionalized by the length of the beam, $x^* = \frac{x}{L}$. By these dimensionless parameters all partial derivatives of the deflection and external forces on the beam are non-dimensionalized. The frequency representation used to non-dimensionalize all time-based variables is chosen to best represent the properties that influence the natural frequency of oscillation of the beam.

$$u_t^* = \frac{u_t}{\omega L}, \quad u_{(tt)^*}^* = \frac{u_{tt}}{\omega^2 L}, \quad u_{(xxxx)^*}^* = L^3 u_{xxxx}$$

It is important to note that all forces in this equation of motion are expressed per unit length of the beam.

With all terms in the Euler-Bernoulli beam equation represented in dimensionless parameters, the unknowns of the equation do not prevent the equation solution. The Runge-Kutta model provides a ready approximation of the behavior of the beam with all forces accounted for. Note that the coefficient chosen for viscous damping was modeled directly based on experimental data of the beam sample settling times. While this is a brute-force and direct method, more sophisticated calculations are available to determine the damping coefficient as stated in[?]lee). After finding the solution of the beam equation in terms of position and velocity, much insight into the factors influencing the motion of the beam is gained. Not only is this dimensionless equation useful for modeling the dynamic behavior of the flexible electrode, but an accurate magnitude of dominant parameters is also attained broadening the perspective gained upon a look into influential parameters. Further implementation of analysis and data processing yields results to compare alongside experimental results. In this study, this processing is carried out

by FFT for frequency domain analysis, frequency and voltage comparisons, as well as discussion of phase plots. Such is useful for validating parameters such as the damping coefficient in the numerical model.

Chapter 2

Experiments

2.1 The Setup

The experiment consists of an In₂O₃/Au/Ag coated polyester [PET] film, where the particulate second-phase is deposited to one side of the film. The film is cantilevered clamped on one end to an insulated podium, sized to allow for reasonable gap lengths as a flexible continuum electrode, and free at the other end. A rigid metal alloy bar is chosen for the stationary ground electrode upon the assumption of its higher conductivity than that of the film (which is useful when serving as the stator electrode); cylindrical risers under the metal alloy bar impose gap lengths that are useful for electrostatic actuation. The gap lengths used for adequate actuation of the $L = 100\text{mm}$ film specimen are $a = 45\text{mm}$ and 48mm for the non-linear and linear experiments, respectively; for the $L = 150\text{mm}$ film specimens $a = 67\text{mm}$ and 69mm gap lengths are used for the non-linear and linear experiments, respectively.

The flexible and rigid continuum structures are configured in an open circuit as parallel plates. A high voltage power supply and Spellman amplifier are utilized for voltage and current regulation. Current is maintained in the milli-ampere range to allow for safe operation at high voltage and low resistance in the open circuit. Wave forms are produced by an Agilent wave

Table 2.1: Table of parameters

Parameter	Value
Density of I2O3/Au/Ag polyester film (ρ)	1185 $\frac{kg}{m^3}$
Modulus of elasticity of I2O3/Au/Ag polyester film (E)	3.4 MPa
Permittivity of free space (ϵ_0)	8.854×10^{-12}
Relative permittivity (dielectric constant, ϵ_r) for air	1

form generator; due to the specificity of signal types, the generator allows for multi-parameter wave forms. A Pixelink CCD high speed camera captures the dynamic motion of the apparatus for analysis. To enhance visibility for data collection, a halogen-bulb desk lamp was placed in view of the CCD camera, behind the two electrodes. This experimental set-up comparatively agrees with those used in previous studies [6, 9]. Fig. 2.1 diagrams the apparatus and supporting elements.

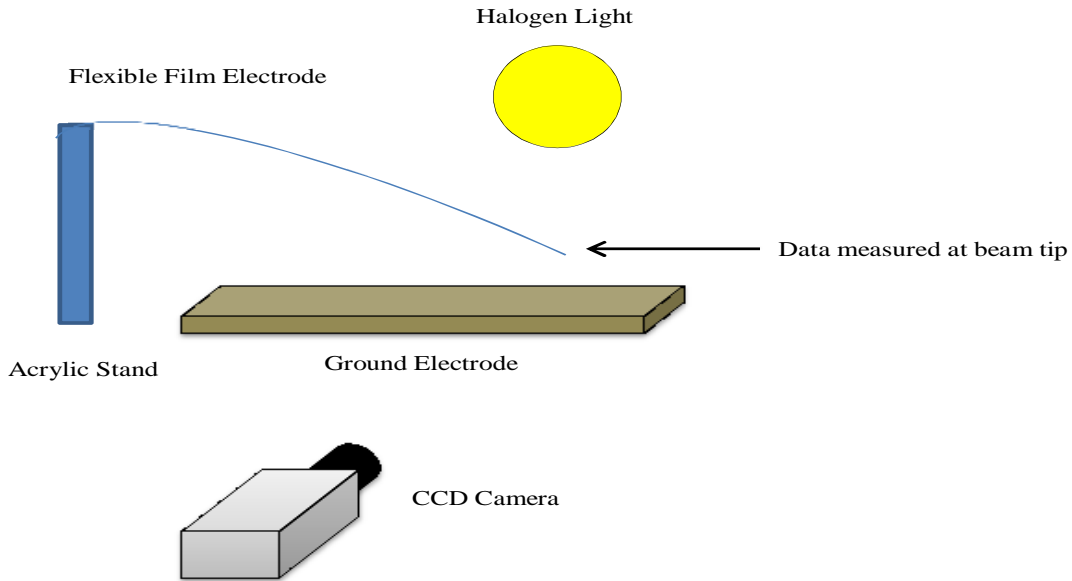


Figure 2.1: Schematic of experimental setup and region of interest used in the analysis

2.2 Procedure

An AC electrical signal is introduced to the circuit where the flexible electrode is at one end and the metal alloy ground electrode is at the other similar to that of a basic voltage source to parallel plate capacitor circuit. The wave form generator is set to apply voltages on the range of 6 to 10 kV at 500V increments for observation of the flexible electrode. It is important to note that voltage levels are maintained below any magnitudes at which pull-in will occur [4, 10, 11]; stripping of the metal particulates from the surface of the film was also avoided by maintaining voltage levels below 12kV. The voltage represented here includes an offset of half of the total amount mentioned, which determines the DC input and AC modulation amplitude where the DC component is the offset and AC component is the amplitude of modulation. In the case of these trials, the DC and AC components of the wave form are equal. The frequency input of the wave form generator is also varied from 0 to 10Hz in 1Hz increments (Note: $\omega = 2\pi f$). After the power supply is initiated, the frequency and voltage are set to specified trial values, and the oscillating motion of the film is observed.

Data collected in this set of experiments includes that of three film geometries to account for influence of the geometry:

13mm X 100mm X 0.2mm, 13mm X 150mm X 0.2mm, and 26mm X 150mm X 0.2mm.

As previously noted in Eq. 1.6 and Eq. 1.7, a sinusoidal alternating wave form and piecewise linear wave form account for the influence of the input signal. A symmetric triangular input is selected for the linear input due to its smooth periodic motion and agreement with the predicted sinusoidal motion of the film as a continuum structure.

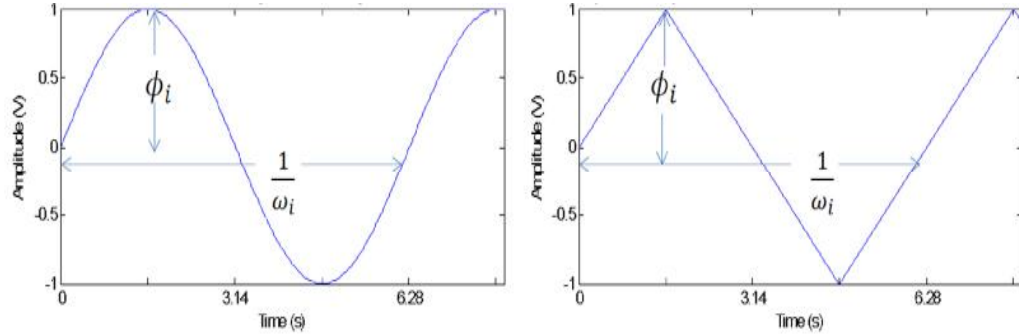


Figure 2.2: Input signals for electrostatic actuation, the first being a sine wave (left) and the second being a triangle wave (right).

2.3 Experimental Analysis Technique

After recording the deflection of the flexible electrode, a simple MATLAB program processes the data. This program gleans a position versus time map of the free end of the flexible electrode for data analysis. This program relies on basic imaging techniques to convert the 800 frames, at 100 frames per second and 320x240 pixel resolution, to a position versus time data set (focusing on the film tip). The digitally captured images contain information of the light intensity, or lack thereof on the range of 0 to 255 0 being the lowest and 255 the highest intensity. Because the thickness of the film in each 8s trial is 3 pixels on average, the position versus time map is scaled by a factor of 200m to 3 pixels. This is equivalent to a 16mm window height for the position versus time maps.

The viscous damping coefficient is experimentally determined by displacing the flexible electrode initially and observing the film return to rest in open ambient air. As seen in Fig. 2.3, the exponential envelope gives a settling time of approximately $t = 20$ s. Within this 20 second window, each value is tested to find if the value is a maximum of the tip displacement function that is greater than the zero value (8000 microns) and less than the maximum amplitude of oscillation (16000 microns). If the value meets these criteria, it is stored in a subset that contains these maximum values of the position versus time function. The natural logarithm is computed for each value of this subset and plotted. MATLABs curve fit function then plots a linear curve

fit to the data which is shown in Fig. 2.4. The slope of this linear curve fit corresponds to a damping coefficient of approximately $c = 2.17 \times 10^{-4}$ N-s/m. Applying this damping to the numerical model, position VS time data yield results consistent with the experimental results.

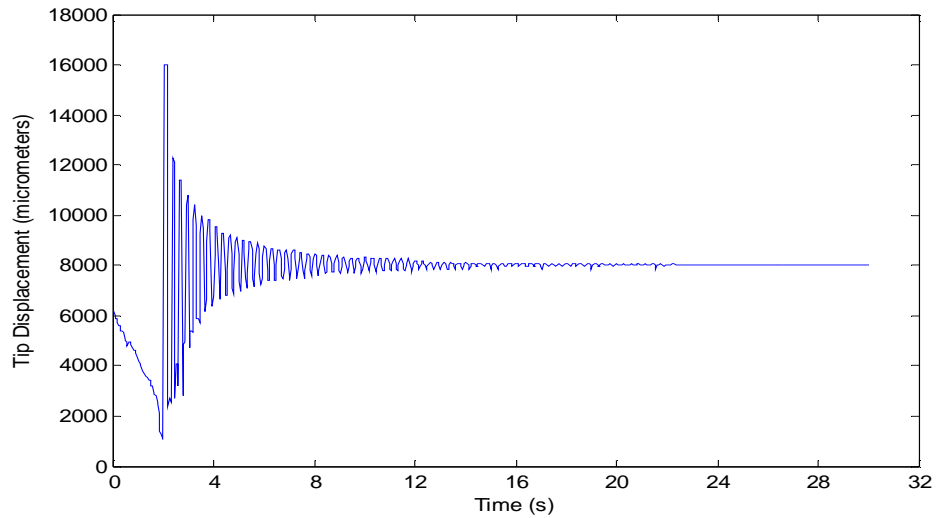


Figure 2.3: Underdamped oscillation of the film used to determine viscous damping coefficient.

2.4 Numerical Analysis

For comparative analysis, a second MATLAB script is employed to extract information concerning the oscillation frequencies of the film when actuated. In this program, the position versus time data is equalized by the mean value of the data set such that the sinusoidal data set passes through the horizontal axis relatively symmetrically. The refined position versus time data is scrutinized for frequency data using the MATLAB FFT function. A noise level is set depending on the resolution of frequencies contained in the position versus time data sets noise floor levels are typically selected at 1 percent or 10 percent of the maximum frequency amplitude (in dB).

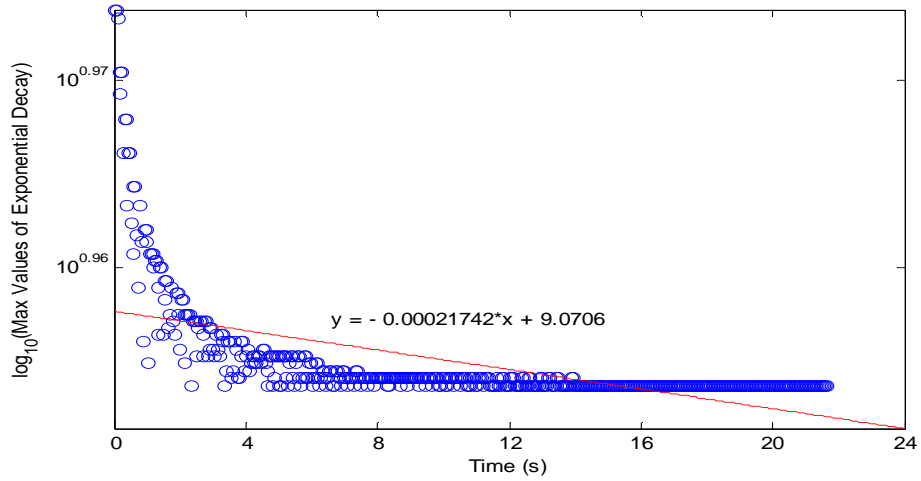


Figure 2.4: Logarithmic curve fit used to determine damping coefficient.

There were some data sets that required a visual inspection of the FFT output to determine the noise level, so all FFT outputs were plotted. Extracted frequency data was stored for use in analysis with respect to voltage and input frequency, where useful information for stability is expositied. An important note for the output frequencies extracted, is that a scaling factor of 1/8 is necessary to convert the FFT output from sample numbers to Hertz values. This is represented in the frequency processing equation:

$$f = \frac{\nu}{NT}$$

where ν is the sample number at which the peak occurs, N is the total number of samples and T is the sample time interval.

For this study, $NT = (800 \text{ samples})(0.01 \text{ seconds per sample}) = 8 \text{ seconds}$.

Lastly, a MATLAB script plots position versus time data on the horizontal axis and velocity versus time data on the vertical axis to form phase diagrams for analysis. To acquire velocity versus time data, the position versus time data entries are iteratively subtracted and divided

by a time interval of 0.01s, following the equation:

$$v_{out} = \frac{u_{out,i} - u_{out,i-1}}{t_i}$$

where $t_i = 1$ for each frame interval of 0.01s. Following a keen analysis of the voltage and frequency influence, as well as the phase plot representations, stability criteria are determined.

Chapter 3

Results from Image Analysis

Experiments were conducted in trials such that the influence of three prominent factors was exposed. These factors were selected on the basis of the magnitude of terms in the non-dimensionalized equation of motion Eq. 1.11, observed for output frequencies, from which we can acquire generalized conclusions on the behavior of oscillation. More significantly, the dominance of the factors studied proves a necessary platform from which a discussion of stability can take place. These factors include:

1. The influence of voltage on the amplitude of oscillation.
2. The influence of input frequency on the position output form.
3. The influence of scale, or geometry, of the film on the position output uniformity.

As common factors of interest, voltage, frequency and geometry also prove practical tools for analysis and discussion of the electromechanical properties of the apparatus. The electrostatic forcing and inertial bending interaction is thus quantified. Future study of the influence of the gravity and damping on the oscillatory motion of the film would prove useful in developing more robust conclusions on oscillation stability. Because the viscous damping opposes the motion of the beam, it would prove and especially useful study when considering anomalies in viscous

media, such as wind gusts and other laminar or turbulent time-dependent events.

3.1 Influence of Voltage

Plots of position versus time for voltage ranging from 6 to 10kV exposes the dependence of oscillation amplitude on the voltage input. Generally speaking, a voltage increase serves to increase the amplitude of oscillation; this verifies with the direct proportionality of the voltage in Eq. 1.11. This also agrees with studies conducted on continuum structures at the micro-scale [5, 6, 7, 8, 9]. Fig. 3.1 illustrates an amplitude increase in position of the film tip due to trials of increased voltage. Because the data set in Fig. 3.1 is near the natural frequency of the 13mm X 150mm X 0.2mm beam, beat phenomenon is exhibited in the beam. This occurs only for the non-linear input signal, as is expected for the interaction of the sinusoidal actuation force and the natural motion of the continuum structure, as governed by Eq. 1.10.

A change in frequency does not affect the general influence of voltage on the oscillations of

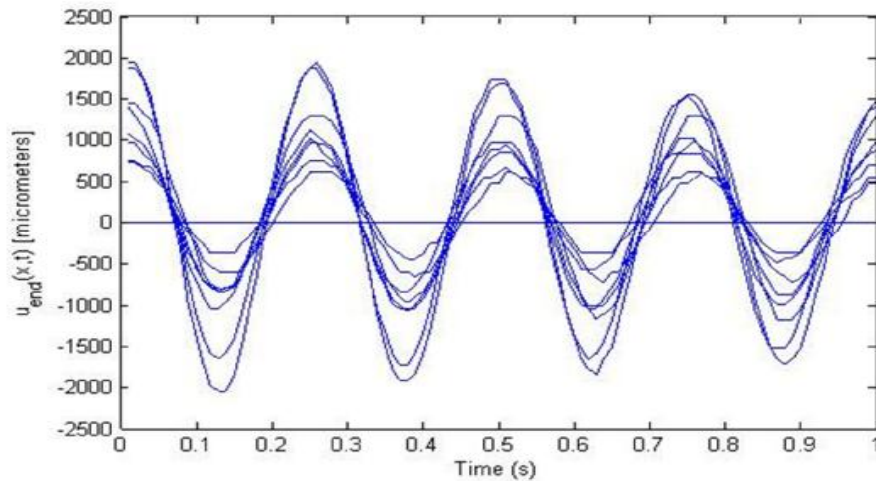


Figure 3.1: Position VS time of the film tip for various voltages (4 Hz, 0-10kV, sinusoidal signal, 13mm X 150mm X 0.2mm).

the film. However in close range of the natural frequency of the film, amplitude of oscillation is greater, whereas outside of the range of the natural frequency amplitude of oscillation is significantly decreased. Data sets indicate that an amplitude of oscillation increase follows as the voltage is increased. This trend is shown in Fig. 3.1. The relationship of the voltage and amplitude of oscillation suggests that the position function of the beam tip also has a increasing relationship with the electric potential. While this is implied in the dimensionless expression, the numerical model is needed to validate this implication.

3.2 Influence of Frequency

As mentioned, the input signal frequency has significant influence on the amplitude of oscillation outside of a close range to the natural frequency of the film configuration for the three cases. Frequency of the signal also changes the wave form of the output function depending on the phase locking interaction of the forcing function with the unforced, natural dynamic motion of the film this is explained using the principle of superposition. Fig. 3.2 illustrates the superposition of two sinusoidal signals, representing a position function of the film tip due to inertial bending based on the properties of the film and a forcing function due to electrostatic actuation of the film by an AC signal.

A sinusoidal signal will impose constructive and destructive influence on the natural motion of the beam in a non-linear fashion. Volatile phase interactions will limit the oscillatory freedom of the film as the input frequency is set further away from the natural frequency of the film. The closer the input frequency is set to the natural frequency of the beam, the greater the opportunity for phase locking to take place. Of course true phase locking will occur when the input frequency is exactly equal to that of the natural frequency of the cantilever film and resonance is observed. Fig. 3.4 shows the phase-locking nature of the film and input signal as the frequency is increased.

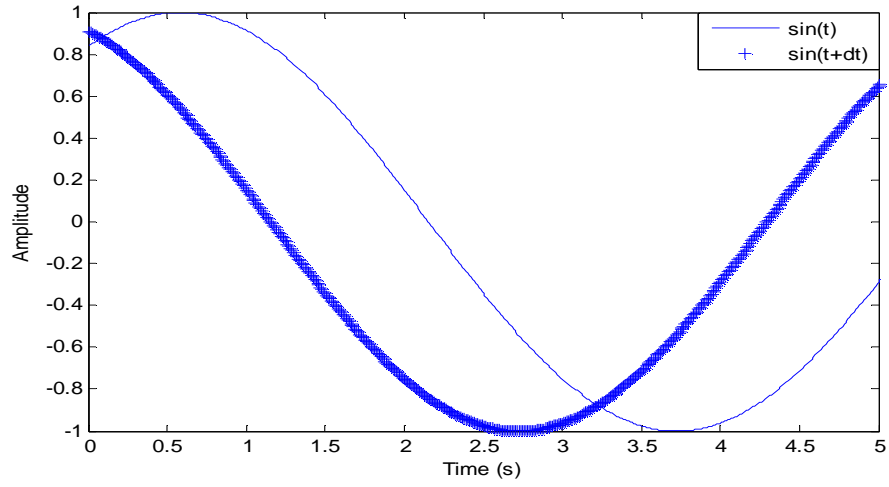


Figure 3.2: Graphical explanation of phase locking for a sinusoidal input signal.

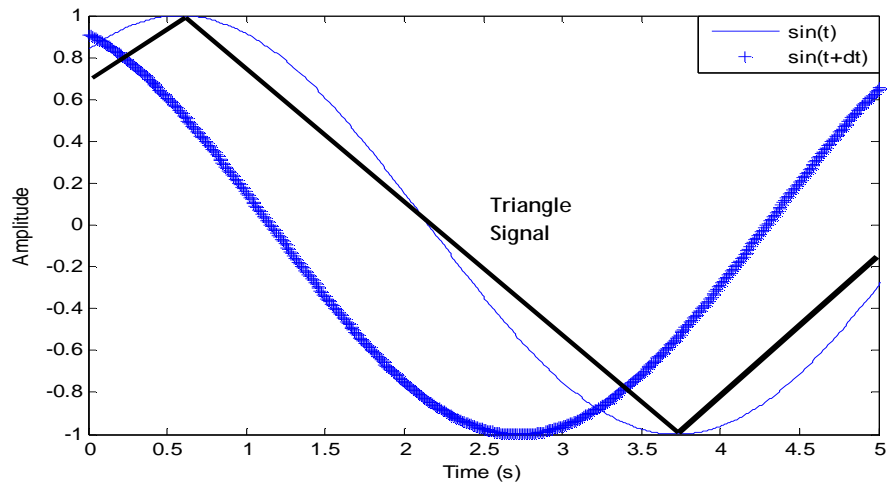


Figure 3.3: Graphical explanation of phase locking for a triangular input signal.

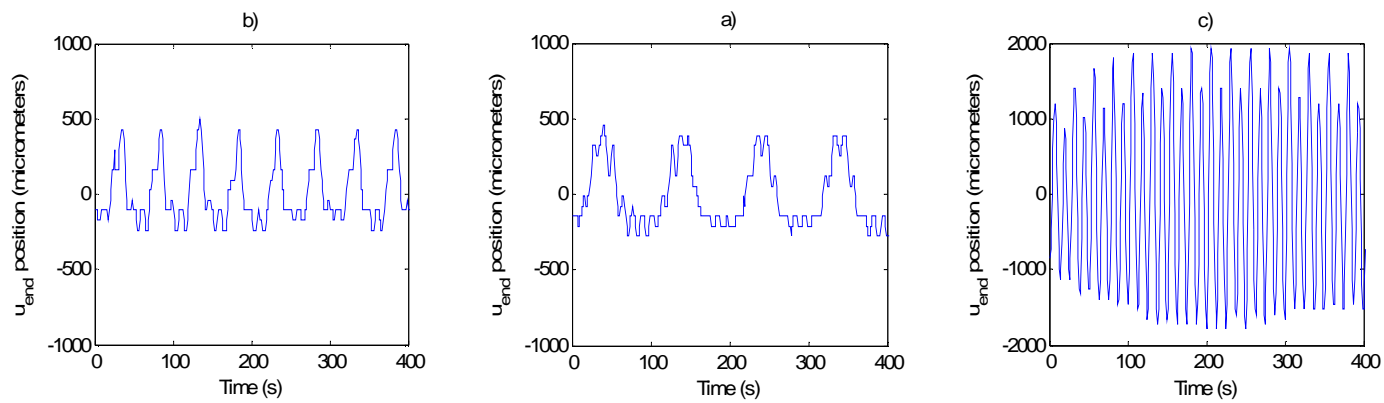


Figure 3.4: Position versus time for the non-linear input: 1Hz (a), 2Hz(b), 4Hz(c) (10kV, 13mm x 100mm, 0.2mm).

For the linear signal input, the constructive and destructive forces are linear and thus conform to the natural motion of the beam as phase locking becomes clear Fig. 3.3. However, the linear signal is dissimilar to the natural motion of the beam outside of a close range of frequencies to the natural frequency of the film. Therefore, the forcing due to the input signal dominates the form of the position output of the film tip. Fig. 3.5 shows influence of the natural frequency embedded in the form of the input signal.

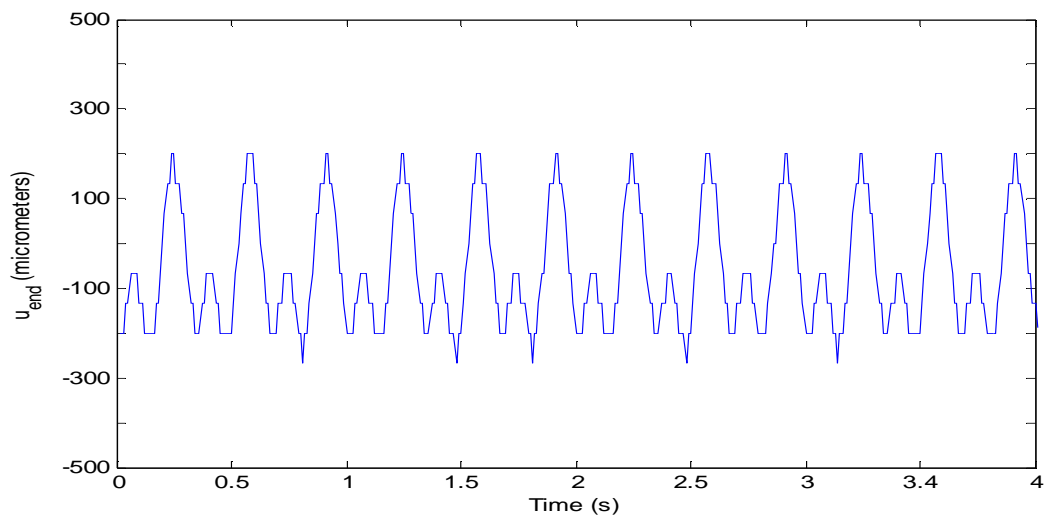


Figure 3.5: Position versus time for the linear input: 3Hz (7kV, 13mm x 100mm, 0.2mm).

3.3 Influence of Scale

The influence of scale is best understood in treating the non-linear and linear signal inputs separately. While the two wave forms do exhibit influence of the properties of the beam i.e. modulus of elasticity, mass, moment of inertia, cross-sectional area the magnitude of that influence is unique to each signal type. Thus, the two will be treated separately and compared

in discussion. Before reviewing the resulting influence of scale, it is useful to scrutinize the resolution of the FFT plots used to produce the scale argument data sets. Fig. 3.6 is a FFT plot of data collected near the natural frequency of the 13mm X 150mm X 0.2mm film specimen at 10kV. For pronounced sample amplitudes such as these, a clear 10% noise floor is adequate. However, a less distinguishable sample amplitude set requires a finer noise floor for accurate data analysis. Despite setting the noise floor to 1% of the maximum sample amplitude, sets of this nature tend to be particularly noisy. This is generally a result of poor phase locking a higher frequency inputs. All film sizes and signal types tend to follow this behavior. From these FFT plots, results for the scale argument are compiled.

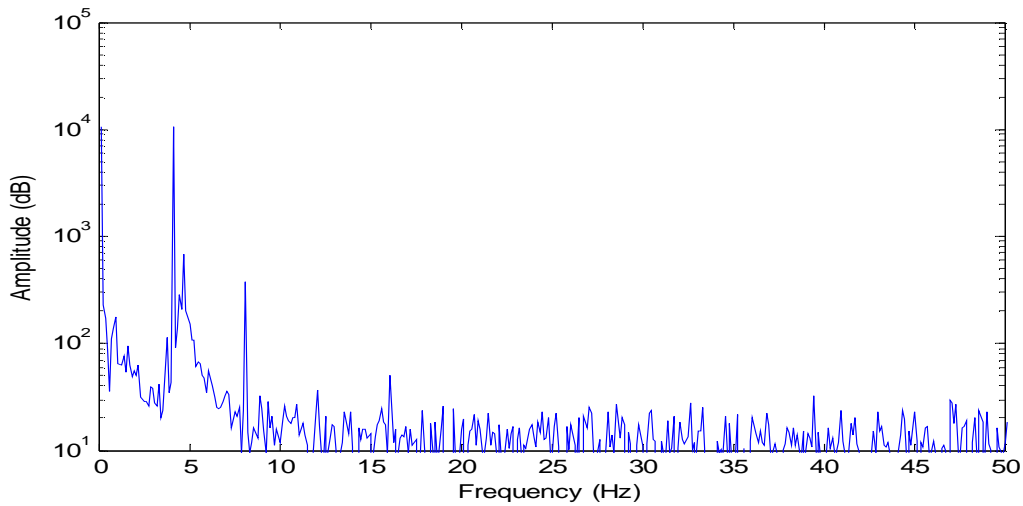


Figure 3.6: FFT plot for 13mm x 150mm x 0.2mm beam at 4Hz and 10kV.

3.3.1 Sinusoidal Signal Data Set

As seen in Fig. 3.4, sinusoidal actuation of the flexible film electrode produces a purely non-linear, trigonometric deflection pattern for all applied voltages and frequencies. Fig. 3.7 is a

graphic representation of the various frequencies induced by applied voltage in the electrostatic forcing.

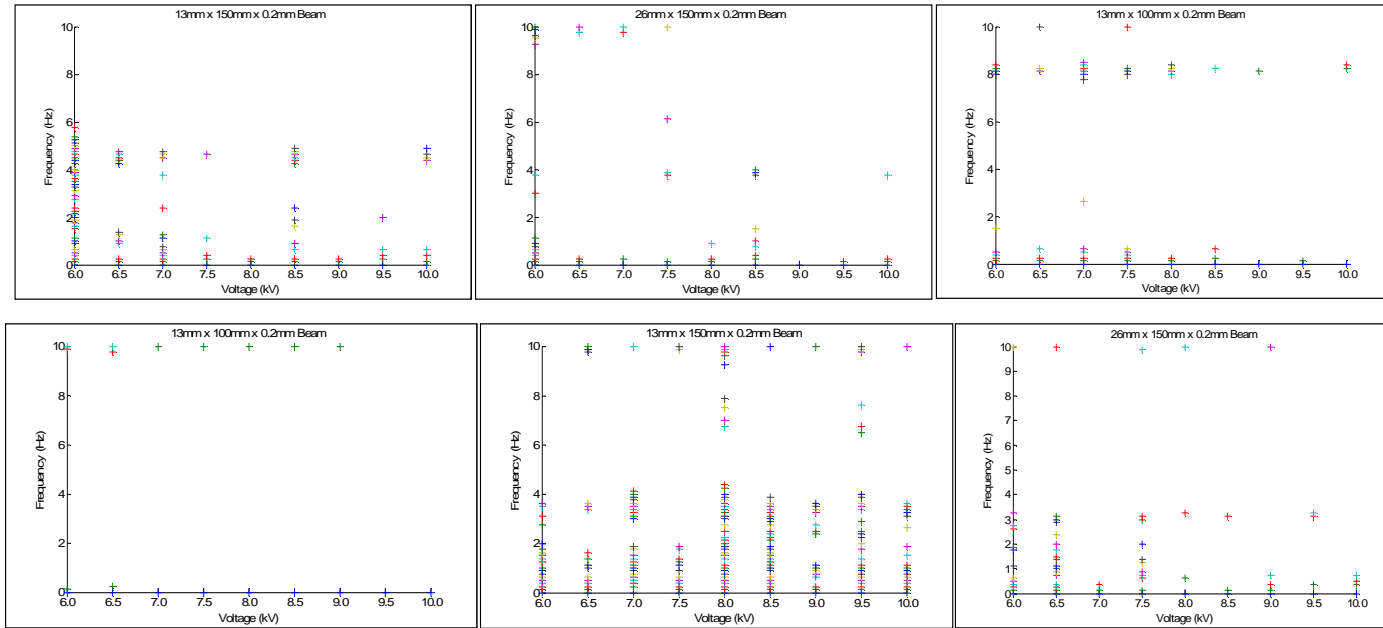


Figure 3.7: Frequency output versus voltage for beam sizes (10Hz, 0-10kV); nonlinear input (top), linear input (bottom).

For an input frequency of 10Hz, the natural frequency of the film dominates the presence of output frequencies contributing to deflection as seen in the top set of graphs. The 13mm X 100mm X 0.2mm film size reveals the dominance of inertial bending in sinusoidal actuation of the film. As the voltage increases the influence of other frequencies including that of the electrostatic forcing becomes inconsequential. Due to a low noise floor, the presence of several other frequencies is apparent in the 13mm X 150mm X 0.2mm data. Nonetheless, the influence of the film properties on its oscillation pattern dominates the frequencies seen. At much lower voltages, the presence of the input frequency is present in the 26mm X 150mm X 0.2mm data. A trend of reduction of inconsequential frequency presence is also seen in this data set as the voltage is increased to 10kV.

3.3.2 Triangular Signal Data Set

Fig. 3.7(bottom row) indicates the result of the linear triangular input signal, and gives insight into the dominance of the inertial forces versus electrostatic force for the triangular input wave form. As previously stated, the forced signal dominates the motion of the beam while the forced frequency is far outside of the range of the natural frequency of the flexible electrode. At 10Hz, the dominance of the forced signal is clearly seen.

For the 13mm X 100mm X 0.2mm film, a high noise floor (10%) removes the presence of weak natural frequency influence. Decreasing the noise floor to 1% of the maximum sample amplitude shows the presence of weak frequency influence in the 13mm X 150mm X 0.2mm beam data. Below a region close to the natural frequency of the beam, there are various frequency influences on par with that of the natural frequency. However, above the natural frequency, the influence of the electrostatic forcing dominates other frequency influence. This trend is also present in the 26mm X 150mm X 0.2mm film specimen data. In agreement with the sinusoidal data sets, this film specimen data also exhibits a decrease of inconsequential frequencies as the voltage is increased. Generally speaking concerning the linear input signal, the inertial bending

has much less influence on the oscillation pattern of the film than that of the non-linear signal. According to the magnitude comparison of the terms in Eq. 1.11, where $\phi(t)$ is represented by the triangular signal of Eq. 1.7, this assertion is valid.

3.4 Numerical Model Results

Generally speaking, the model data conforms to the experimental data sufficiently when considering voltage, frequency and scale. Fig. 3.8 shows the position versus time data for the sinusoidal case, which follows the expected progression.

Fig. 3.9 shows the destructive or constructive influence of frequency and revealing the

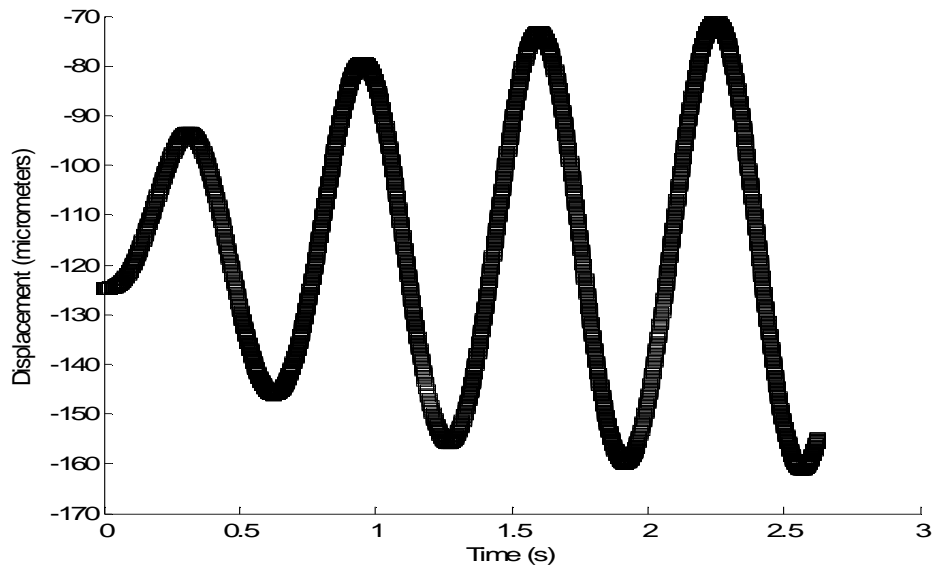


Figure 3.8: Position versus time data for the 13mm X 100mm X 0.2mm specimen at 2Hz and 7kV.

influence of scale on the frequency of the beam for the numerical model as well.

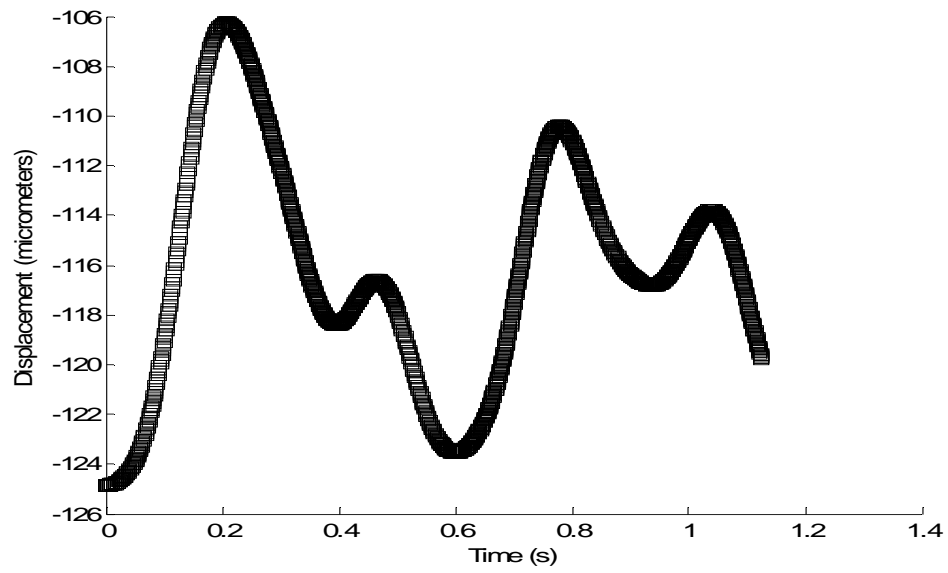


Figure 3.9: Influence of frequency in numerical model for the 13mm X 100mm X 0.2mm specimen at 7Hz and 7kV.

Chapter 4

Discussion

4.1 Frequency Density

For the sinusoidal data, deflection relies on the interaction of the natural frequency (i.e. properties of the composite material of the film) with the frequency and voltage at which the electric field is modulated. Of particular interest when quantifying stability is the interaction of the input frequency and the frequencies produced. Fig. 4.1 plots the density of frequencies induced for all frequency trials of the electrostatic forcing.

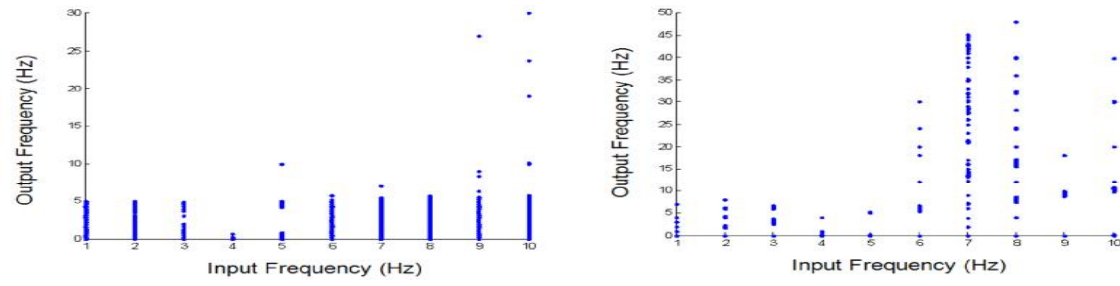


Figure 4.1: Frequency density plots for the 13mm x 150mm x 0.2mm film specimen.

As the input frequency approaches the natural frequency for the 13mm X 150mm X 0.2mm film size, a less dense column of frequency output is apparent. The lessened density of frequencies signifies a lack of the various inconsequential frequencies that are prevalent as the input frequency is set further away from the natural frequency. A lack of such destructive interference to the motion of the film electrode frees the film to exhibit stable deflections. This is best seen in both signal data for the 13mm X 150mm X 0.2mm film when the input frequency is at 4Hz and 5Hz. Recalling Fig. 3.7, the natural frequency for this film geometry occurs close to 4Hz.

As noted in Chapter 3, varying input frequency has a phase-locking relationship with the natural frequency of the film. As the input frequency is varied, the period of oscillation also varies inversely. The interaction of the varying input frequency with the natural frequency of the film causes instabilities in non-resonant frequency excitation. This lack of phase locking is illustrated by the various frequencies associated with unstable oscillation (See Fig. 4.1 - frequency density plot). This is also seen visually in chaotic oscillations of the flexible electrode. Such disagreement of the input and resonant frequency characterizes regions of avoidance when vying for smooth deflections. In the case of the non-linear sinusoidal input, resonance is assumed. i.e. two very similar frequencies (ideally one) are seen, for the given input frequency. The linear signal has a more loosely convergent relationship with the ideal film motion (as dictated by inertial forces only; or the linear homogeneous Euler-Bernoulli partial differential equation). Ideally, a sufficiently phase locked triangular input frequency and natural frequency will smooth the triangular wave form at the peaks and troughs. Also, the sinusoidal inertial bending induced motion and the linear electrostatic induced motion are equal as the two functions cross the horizontal axis. These two interactions cause the linear signal to have a wider range of stability around the natural frequency of the film. This is seen in the less dense columns at 4Hz and 5Hz for the linear signal as opposed to the non-linear signal input. Comparing the frequency densities for the numerical model to those produced by experimentation, the model agrees sufficiently with the experimental data.

4.2 Phase Plots

Considering again the position versus time data, velocity data is extracted using a time difference approach. Fig. 4.2 (left) is the phase diagram of a simple oscillator. Assuming the oscillator exhibits simple harmonic motion, the position data will be that of sinusoids. In turn, an analytical derivative of the position will produce co-sinusoidal velocity data. Plotting position on the horizontal axis and velocity on the vertical axis, the phase map forms a perfect circle. When plotting position data with velocity data for the non-linear input, Fig. 4.2 (center) is produced. Likewise the linear signal data produces Fig. 4.2 (right).

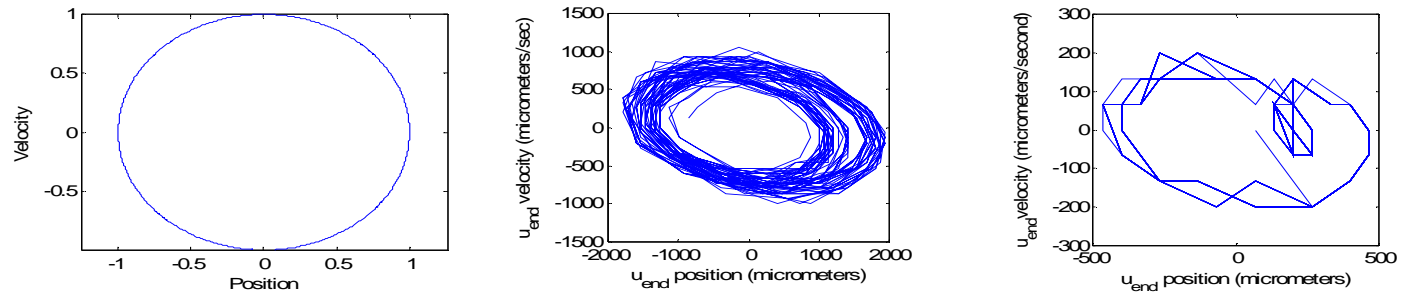


Figure 4.2: Phase plot graphs for a simple oscillator (left), sinusoidal signal (center), and triangular signal (right) 13mm X 100mm X 0.2mm beam, 4hz, 10kV.

It is important to note that the lack of phase locking and presence of unstable motion, some phase diagrams for various voltage and frequency data are not useful for discussion. This behavior is seen best in high voltage data that is far outside of a close range to the natural frequency.

The shape of the phase diagrams for both the non-linear and linear signal data appear elliptical in shape. This is due to the dependency of the electrostatic actuation force on the gap length separating the flexible film electrode and the rigid ground electrode. The electric field that produces the electrostatic force has an intensity that relies on the distance of the gap between the two electrodes (as in the case of an ideal capacitor configuration). Because the field has a tendency to push the film the most at the bottom of its oscillation (when the gap length is at its smallest value), the velocity increases to a maximum quickly. This behavior is displayed in the general trend of an increase in velocity at a decreasing rate as the film deflection reaches the center of its stroke height. The film continues its path as the velocity decreases to the top of the film stroke height; here the gap length is at its maximum and the electric field intensity is at its minimum. As the film continues back to the center of its stroke a less pronounced pull is apparent and thus verifies that the electric field changes direction and pulls the film back to the lowest point in its stroke.

The non-linear signal appears smooth and has greater amplitude of oscillation than that of the linear signal. This presents important implications when considering stability versus greatest oscillation amplitude. Because the non-linear signal is most favorable for phase-locking, the sinusoidal case yields higher amplitude of oscillation. However, the linear signal has a greater window of opportunity for stability to take place, which is illustrated again in the less dense phase diagram Fig. 4.2 (right). Comparing the experimental phase plots with that of the numerical model shows agreement of the two for the sinusoidal and triangular signal cases.

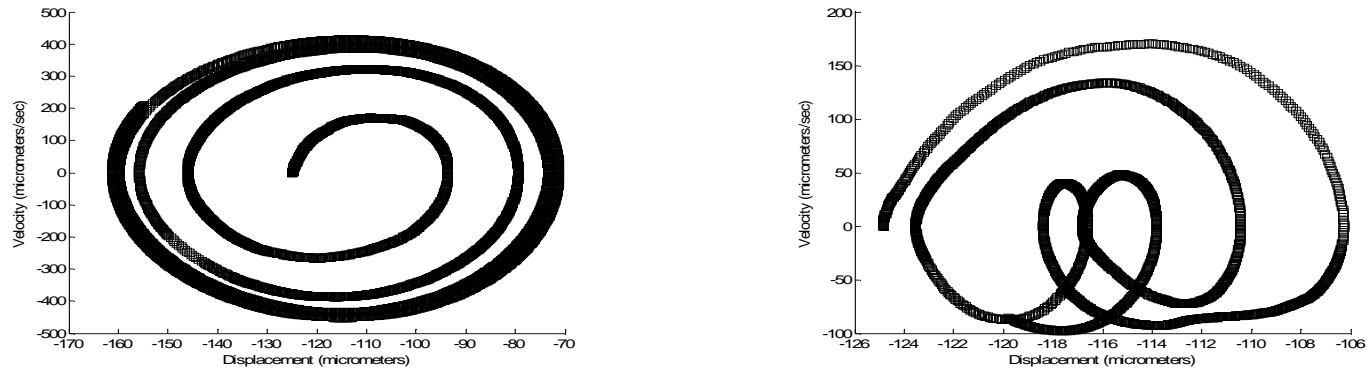


Figure 4.3: Phase plot graphs for the numerical model sinusoidal signal 3Hz (left) and 7Hz (right) at 7kV 13mm X 100mm X 0.2mm film specimen.

In the following section results obtained from the solution of the numerical model is compared with actual experimental values in an error analysis; this is followed by conclusions.

Chapter 5

Error Analysis

The differences seen in numerical model data and experimental data warrant an error analysis – to make note of conformity of the model to reality. The probable causes of errors being introduced in the analysis are

1. Assuming constant gap distance separating electrodes.
2. Environmental irregularities.
3. Resolution of CCD camera.

The difference in magnitude and form for each data set is caused by the assumption that the gap distance does not change for the numerical model. Introducing a varying gap distance into the electrostatic forcing term of the Euler-Bernoulli beam equation causes linearity that is not addressed in the assumptions noted. Also, differences in environmental conditions may have caused data to skew to some extent. Wind gusts from air-conditioning vents and external vibrations could be reduced to obtain more accurate data. Such anomalies cannot be predicted. Lastly, the resolution of the videos captured by the CCD camera create a noise floor for data collection. This noise floor can distort data the is processed for analysis and give an impression of more dominating frequencies influencing oscillation than reality.

Chapter 6

Conclusions

This study is based on delineating criteria by which stability is achieved in an electrostatically actuated flexible electrode. Because an AC electric potential supplies the electric field by which the film electrode is actuated, a sinusoidal signal is compared with that of a triangular signal. These two signal types are synonymous with an electrostatic forcing function in the Euler-Bernoulli dynamic beam equation discussed in Chapter 1 composed of a non-linear sinusoidal component or a linear piecewise component, respectively. Experiments conducted utilizing these two signals also include consideration of voltage, input signal frequency and scale influence on the induced oscillation of the flexible electrode.

Trials were recorded by capturing the motion of the free end of the cantilevered film using the CCD camera. Afterwards, MATLAB data processing scripts were employed to present the trials in a manner in which they could be studied. First quantifying the influence of voltage, an increase in electric field intensity and subsequently an increase in oscillation amplitude, is the result of voltage increase. For stable high-amplitude deflection, this is the first step. As the frequency approaches the natural frequency of the film, stable oscillation ensues. Non-linear sinusoidal forcing produces higher amplitude oscillations but also various harmonics and destructive frequency influences into the oscillation except when the input frequency is nearest to

the natural frequency of the beam. However, a linear signal produces lower amplitude oscillations as well as less harmonics and destructive frequency influence. Despite its lower oscillation amplitude the high influence of the input signal allows for a broader opportunity for stable vibration. Outside of a range of 2Hz, the destructive nature of the lack of phase locking is seen and the film oscillates in an unstable manner. The scale of the film dominates the oscillation of the non-linearly actuated film, but has less influence on the movement of the linearly actuated film.

Analyzing the density of frequencies present in the motion of the film when actuated by the two signal types, the linear signal is found to produce less dense frequency data at the input frequency values surrounding the value of the natural frequency. The range of notable stability (presence of 3 or less frequencies) around the natural frequency of the cantilevered film that is linearly actuated is considerably larger than the region of notable stability for non-linear actuation. Future work to quantify this range will prove quite useful. The phase plots presented corroborate this discovery and introduce the influence of the non-uniformities in the electrostatic field modulation. Though the non-uniformity does not affect the stability of the film in an appreciable manner, the non-uniformities seem to couple well with the non-linear actuation and produce higher amplitude of oscillation at faster velocities. Again however, the linear signal produces a less dense map that favors stability at a wider range.

Future studies will include further geometry-based experiments to find the influence of non-linear and linear signals on more complex geometries. Likewise, experiments with simulated and replicated bio-signals will offer insight into stability for flapping film electrodes. Further quantification of the influence of electrostatic actuation on the whole of the film length would also be useful in validation of the results presented. Wind gust testing will provide useful data for recommending the use of linear actuation in fluid medium phenomena. Finally, a computational model to support the analytical model presented is needed to quantify the influence

of each component presented in the dimensionless equation of motion, observed for output frequencies (Eq. 1.11). Predicting the influence of these components accurately could provide a useful design tool upon which stability criteria can be based. Assuming that small birds such as a hummingbird uses listening functions of the brain to process stable flight patterns and wing-beat frequencies, a control system for a bio-mimetic drone can be designed around this concept taking advantage of the wider range of stability offered by the triangular signal to regulate flapping patterns. Using this model applications in heat transfer by means of a planar fan can also be validated, design of cleaning and valve motion are possible in biomedical applications, and optimization with a pivoting boundary (as opposed to a fixed) will better mimic flapping wing dynamics of winged fauna.

REFERENCES

- [1] J. D. Jackson, *Classical Electrodynamics*, John Wiley and Sons Inc, New York, 1999.
- [2] D. J. Griffiths, *Introduction to Electrodynamics*, Prentice Hall, New Jersey, 1999.
- [3] P. Decuzzi, A. Granaldi, G. Pascazio, Dynamic response of microcantilever-based sensors in a fluidic chamber, *Journal of Applied Physics* 101 (2007) 024303–1–024303–6.
- [4] F. D. Bona, E. T. E. (Eds.), *Microsystems mechanical design. CISM courses and lectures No. 478*, International Centre for Mechanical Sciences, Springer Wien, New York, 2006.
- [5] R. C. Batra, M. Porfiri, D. Spinello, Review of modeling electrostatically actuated micro-electromechanical systems, *Smart Materials and Structures* 16 (2007) R23–R31.
- [6] A. Ballestra, E. Brusa, M. G. Munteanu, A. Som, Experimental characterization of electrostatically actuated in-plane bending of microcantilevers, *Microsystem Technologies* 14 (2008) 909–918.
- [7] S. Chatterjee, G. Pohit, A large deflection model for the pull-in analysis of electrostatically actuated microcantilever beams, *Journal of Sound and Vibration* 322 (2009) 969–989.
- [8] B. McCarthy, G. G. Adams, N. E. McGruer, D. Potter, A dynamic model including contact bounce of an electrostatically actuated micro-switch, *Journal of Micromechanical Systems* 11 (2002) 276–283.
- [9] J. Lee, S. Lee, C. Yao, W. Fangi, Comments on the size effect on the microcantilever quality factor in free airspace, *Journal of Micromechanics and Microengineering* 17 (2007) 139–146.
- [10] S. Krylov, N. Dick, Dynamic stability of electrostatically actuated initially curved shallow micro beams, *Continuum Mechanics and Thermodynamics* 22 (2010) 445–468.
- [11] V. Rochus, D. Rixen, J. Golinval, Electrostatic coupling of mems structures: transient simulations and dynamic pull-in, *Nonlinear Analysis* 63 (2005) e1619–e1633.
- [12] H. H. Yoo, K. Jung, S. Moon, Modal and stability analysis of a micro-beam structure actuated by electrostatic force, *Materials Science Forum* 505-507 (2006) 403–408.
- [13] R. J. Wootton, Invertebrate paraxial locomotory appendages: design, deformation and control, *Journal of Experimental Biology* 202 (1999) 3333–3345.
- [14] D. L. Altshuler, K. C. Welch, B. H. Cho, D. B. Welch, A. F. Lin, W. B. Dickson, M. H. Dickson, Neuromuscular control of wingbeat kinematics in annas hummingbirds (*calypte anna*), *Journal of Experimental Biology* 213 (2010) 2507–2514.
- [15] T. L. Daniel, S. A. Combes, Flexible wings and fins: bending by inertial of fluid-dynamic forces?, *Integrative and Comparative Biology* 42(5) (2002) 1044–1049.

- [16] S. A. Combes, Wing flexibility and design for animal flight, Ph. D. Diss, University of Washington, 2002.
- [17] S. A. Combes, T. L. Daniel, Shape flapping and flexion: wing and fin design for forward flight, *Journal of Experimental Biology* 204 (2001) 2073–2085.

APPENDICES

Appendix A

Non-dimensionalization of the Euler-Bernoulli Beam Equation

A.1 Non-dimensional Analysis

The Euler-Lagrange equation for the dynamic motion of a continuum structure described by the Euler-Bernoulli beam relation is,

$$\rho A \frac{\partial^2 u}{\partial t^2} = -EI \frac{\partial^4 u}{\partial x^4} + \sum F_{ext} \quad (\text{A.1})$$

where

$$u = u(x, t)$$

Including the external forces, Eq. A.1 becomes

$$\rho A \frac{\partial^2 u}{\partial t^2} = -EI \frac{\partial^4 u}{\partial x^4} - \frac{c}{L} \frac{\partial u}{\partial t} - \rho A g + \frac{\phi^2(t) b \epsilon_r \epsilon_o}{a^2 L} \quad (\text{A.2})$$

where,

$$\phi(t) = \phi_1(1 + \sin \omega_i t)$$

and

$$\phi(t) = \phi_1^2(1 + 2 \sin \omega_i t) + \sin^2 \omega_i t$$

Choosing the spatial variable to be dimensionless when proportioned with the length of the beam and the temporal variable to be dimensionless when proportioned with a frequency, the dimensionless position and time are,

$$x^* = \frac{u}{L}$$

and

$$t^* = \omega t$$

respectively.

Non-dimensionalization of derivatives in these variables proceeds as follows:

$$\frac{t^*}{t} = \omega = \frac{\partial t^*}{\partial t}$$

and

$$\frac{\partial}{\partial t} = \frac{\partial}{\partial t} \frac{\partial t^*}{\partial t^*} = \frac{\partial t^*}{\partial t} \frac{\partial}{\partial t^*} = \omega \frac{\partial}{\partial t^*}$$

thus,

$$\frac{\partial^2}{\partial t^2} = \frac{\partial}{\partial t} \left(\frac{\partial}{\partial t} \right) = \omega \frac{\partial}{\partial t^*} \left(\omega \frac{\partial}{\partial t^*} \right) = \omega^2 \frac{\partial^2}{\partial t^{*2}}$$

Likewise

$$\frac{x^*}{x} = \frac{1}{L} = \frac{\partial x^*}{\partial x}$$

and

$$\frac{\partial}{\partial x} = \frac{\partial}{\partial x} \frac{\partial x^*}{\partial x^*} = \frac{\partial x^*}{\partial x} \frac{\partial}{\partial x^*} = \frac{1}{L} \frac{\partial}{\partial x^*}$$

thus,

$$\frac{\partial^4}{\partial t^4} = \frac{\partial}{\partial x} \left(\frac{\partial}{\partial x} \left(\frac{\partial}{\partial x} \left(\frac{\partial}{\partial x} \right) \right) \right) = \frac{1}{L} \frac{\partial}{\partial x^*} \left(\frac{1}{L} \frac{\partial}{\partial x^*} \left(\frac{1}{L} \frac{\partial}{\partial x^*} \left(\frac{1}{L} \frac{\partial}{\partial x^*} \right) \right) \right) = \frac{1}{L^4} \frac{\partial^4}{\partial x^{*4}}$$

The length of the beam is again selected to express the deflection of the beam, $u(x, t)$, as a dimensionless quantity

$$u^* = \frac{1}{L}u$$

or

$$u = Lu^*$$

Rearranging coefficients and non-dimensionalizing Eq. A.2:

$$\omega^2 L \frac{\partial^2 u^*}{\partial t^{*2}} = -\frac{EI}{\rho A} \left(\frac{1}{L^3} \frac{\partial^4 u^*}{\partial x^{*4}} \right) - \frac{c}{\rho AL} \left(\omega L \frac{\partial u^*}{\partial t^*} \right) - g + \frac{\phi^2(t) b \epsilon_r \epsilon_o}{a^2 \rho AL} \quad (\text{A.3})$$

Let

$$\omega^2 = \frac{EI}{\rho AL^4}$$

Non-dimensionalizing all terms of Eq. A.3 by the acceleration, $\omega^2 L$:

$$\frac{\partial^2 u^*}{\partial t^{*2}} = -\frac{\partial^4 u^*}{\partial x^{*4}} - \frac{c}{\omega \rho AL} \frac{\partial u^*}{\partial t^*} - \frac{g}{\omega^2 L} + \frac{\phi^2(t) b \epsilon_r \epsilon_o}{a^2 \omega^2 \rho AL^2} \quad (\text{A.4})$$

Appendix B

MATLAB Code

B.1 Data Extraction from Videos

```
if descend2dir == 1
    s1=strrep('dec19_short_xv_z.avi','z',num2str(1));
    s3=strrep('data_dec19_short_xv_z','z',num2str(1));
    thresh=70;
elseif descend2dir == 2
    s1=strrep('dec21_long_xv_z.avi','z',num2str(1));
    s3=strrep('data_dec21_long_xv_z','z',num2str(1));
    thresh=70;
elseif descend2dir == 3
    s1=strrep('dec15_wide_xv_z.avi','z',num2str(1));
    s3=strrep('data_dec15_wide_xv_z','z',num2str(1));
    thresh=140;
end

x0=100;
```

```

volt_start=0; % making data set for the 0v video!
i=1;
s2=strcmp(s1, 'x', num2str(500*(i-1)+volt_start));
s4=strcmp(s3, 'x', num2str(500*(i-1)+volt_start));
x=aviinfo(s2);
y=struct2cell(x);
%note the curly brackets!
fps=y{5};
num_frames=y{4}

for j=1:num_frames
    j
    m=aviread(s2, j);
    [a, b]=frame2im(m);
    pos=beam_end(a, x0, thresh);
    pos_out(j)=pos*(200/3);
    clear pos
end

save(s4, 'pos_out', 'fps')

if descend2dir == 1
movefile(sprintf('data_dec19_short_%dv_%d.mat', 500*(i-1)
+volt_start, 1), './data')
elseif descend2dir == 2
movefile(sprintf('data_dec21_long_%dv_%d.mat', 500*(i-1)+
volt_start, 1), './data')

```

```

elseif descend2dir == 3
    movefile(sprintf('data_dec15_wide_%dv_%d.mat',500*(i-1)+
        volt_start ,1) , './data ')
end

clear pos_out

volt_start=6000;% making data for all other voltatges!

for i=1:9
    s2=strrep(s1 , 'x' ,num2str(500*(i-1)+volt_start));
    s4=strrep(s3 , 'x' ,num2str(500*(i-1)+volt_start));
    x=aviinfo(s2);
    y=struct2cell(x);
    %note the curly brackets!
    fps=y{5};
    num_frames=y{4}

    % m=aviread(s2 ,1);
    % [a , b]=frame2im(m);
    % image(a)
    % pause

    for j=1:num_frames
        j
        m=aviread(s2 , j);
        [a , b]=frame2im(m);
        pos=beam_end(a ,x0 , thresh);
    end

```

```

        pos_out(j)=pos*(200/3);
        clear pos
    end

    save(s4, 'pos_out', 'fps')
    if descend2dir == 1
        movefile(sprintf('data_dec19_short_%dv_%d.mat', 500*(i-1)
            +volt_start, 1), './data')
    elseif descend2dir == 2
        movefile(sprintf('data_dec21_long_%dv_%d.mat', 500*(i-1)+
            volt_start, 1), './data')
    elseif descend2dir == 3
        movefile(sprintf('data_dec15_wide_%dv_%d.mat', 500*(i-1)+
            volt_start, 1), './data')
    end
    clear pos_out

end

```

Appendix C

MATLAB Code

C.1 Data Analysis

```
clear all
close all
clc

if descend2dir == 1
    s1=strrep('data_dec19_short_xv_z','z',num2str(1));
    s3=strrep('freq_data_dec19_short_xv_z','z',num2str(1));
    load(sprintf('data_dec19_short_0v_%d',1));
elseif descend2dir == 2
    s1=strrep('data_dec21_long_xv_z','z',num2str(1));
    s3=strrep('freq_data_dec21_long_xv_z','z',num2str(1));
    load(sprintf('data_dec21_long_0v_%d',1));
elseif descend2dir == 3
    s1=strrep('data_dec15_wide_xv_z','z',num2str(1));
    s3=strrep('freq_data_dec15_wide_xv_z','z',num2str(1));
```

```

        load(sprintf('data_dec15_wide_0v_%d',1));
    end

pos_0v = pos_out;
clear pos_out

volt_start=6000;
hold on
for i=1:9
    s2=strrep(s1,'x',num2str(500*(i-1)+volt_start));
    s4=strrep(s3,'x',num2str(500*(i-1)+volt_start));
    load(s2)
    pos_out = (200/3)*(pos_out - mean(pos_out));
    pos_out(end)=0;

    y=abs(fft(pos_out));
    %figure
    %plot(y)
    noise=0.1*max(y(2:length(y)));

    k=1;
    for j=1:length(y)
        if(y(j) > noise)
            subfreq_out(k)=j;
            amp_out(k)=y(j);
            k=k+1;
        end
    end
end

```

```

        end
    end
    subfreq_out = (subfreq_out - 1) / 8; %corrects the error due to the
        zero point
    %plot(500*(i-1)+volt_start, subfreq_out(1:(length(subfreq_out)-1)
        /2), '+' ) %plots voltage vs frequency
    plot(1, subfreq_out(1:(length(subfreq_out)-1)/2), '.b')
    save(s4, 'pos_out', 'y', 'amp_out', 'subfreq_out')
    clear pos_out y subfreq_out amp_out

end

%saveas(gcf, sprintf('Voltage_vs_frequency_%dhz', l), 'fig');

```

C.2 Phase Mapping

```

% Phase maps of position versus velocity

clear all
close all
format long

s1='data_dec19_short_xv_4';

volt_start=6000;

for i=1:9
    s2=strrep(s1, 'x', num2str(500*(i-1)+volt_start));

```

```
load(s2)
pos_out = (200/3)*(pos_out - mean(pos_out));

% Builds phase map
for j=1:799
    vel_out(i,j) = (pos_out(1,j+1)-pos_out(1,j))/(1);
end

vel_out(i,800) = vel_out(1,799);

figure
plot(pos_out, vel_out(i,:))
axis square
end
```

Appendix D

Code

D.1 Fourth-order Runge-Kutta Model of Non-dimensionalized Beam

```
function [pos_out , vel_out]=Euler_Bernoulli_RKM4(Beam_Length ,  
    Beam_Width , Beam_Thickness , Elastic_Modulus , Beam_Density , ...  
    Damping_Coefficient , Voltage , Modulation_Frequency ,  
    Electrode_Separation_Distance , Grid_Points , ...  
    Tolerance , Number_Periods , Data_Increment)  
  
Beam_Length = input('Length of the flexible electrode: ');  
Beam_Width = input('Width of the flexible electrode: ');  
Beam_Thickness = input('Thickness of the flexible electrode: ');  
Elastic_Modulus = input('Modulus of Elasticity of the flexible  
    electrode: ');  
Beam_Density = input('Density of the flexible electrode: ');  
Damping_Coefficient = input('Damping Coefficient based on  
    environment: ');
```

```
Voltage = input('DC Voltage applied (half of the total voltage): ');
Modulation_Frequency = input('Input Frequency: ');
Electrode_Separation_Distance = input('Gap Distance between the
    flexible/ground electrode: ');
Grid_Points = input('Grid Points: ');
Tolerance = input('Tolerance: ');
Number_Periods = input('Number of periods: ');
Data_Increment = input('Data Increments: ');
```

```
%Beam length in meters
```

```
L=Beam_Length;
```

```
%beam width in meters
```

```
w=Beam_Width;
```

```
%beam thickness in meters
```

```
th=Beam_Thickness;
```

```
%elastic modulus in Pa
```

```
E=Elastic_Modulus;
```

```
%beam density in kg/m3
```

```
rho=Beam_Density;
```

```
%damping parameter which is a function of fluid viscosity
```

```
mu=Damping_Coefficient/L;
```

%area moment of inertia

$I_{xy}=w*(th^3)/12;$

%gravitational acceleration constant in m/s^2

$g=9.81;$

%beam mass

$m=rho*th*w*L;$

%modulation frequency in Hz which is the natural frequency

$\omega=\mathbf{sqrt}((E*I_{xy})/(rho*th*w*(L^4)));$

Natural_Frequency= $\omega;$

Natural_Frequency

%electric permittivity of free space in MKS units

$\epsilon_0=8.854e-12;$

%electric permittivity constant

$\epsilon=1;$

%electric potential constant in volts

$\phi_0=Voltage;$

%distance between electrodes in meters

$a=Electrode_Separation_Distance;$

%Number of grid points not including the boundaries

n=Grid_Points;

%Grid spacing

dx=1/(n+1);

%Grid

x=[0:dx:1];

%scaling for initial condition

W_g=m*g*L^2/(E*Ixy);

%—— Dimensionless variables ——

%dimensionless elastic modulus

B1=E*Ixy/(rho*th*w*(omega^2)*(L^4));

%dimensionless viscous damping

B2=mu/(rho*th*w*omega);

%dimensionless gravitational force

F_g=g/(L*(omega^2));

%dimensionless electrical force

F_e=(phi_0^2)*w*e0*e/((m)*((a*omega)^2)*L);

%electrical modulation frequency in Hz

mod_freq=Modulation_Frequency/omega;

%dimensionless amplitude of the displacement

B4=0.d0;

%Initial conditions below (displacement and velocity)–

%displacement

u(1:n+2)=-(W.g/24)*(x.^4-4*x.^3+6*x.^2);

%velocity

v(1:n+2)=0;

%——Boundary conditions——

%——displacement——

%wall

u(1)=0;

[c,T]=TT([0 1 2 3],1);

u(2)=-(c(1)*u(1)/c(2))-(c(3)*u(3)/c(2))-(c(4)*u(4)/c(2));

%free end

```

[d,T]=TT([-3 -2 -1 0],2);
[e,T]=TT([-3 -2 -1 0],3);

s_factor=1/(1-(d(1)/d(4))*(e(4)/e(1)));

u(n+2)=s_factor*(((d(1)/d(4))*(e(3)/e(1)))-(d(3)/d(4)))*u(end-1)+...
        s_factor*(((d(1)/d(4))*(e(2)/e(1)))-(d(2)/d(4)))*u(end-2);

%velocity
v(1)=B4;

%Time increment
dt=0.3*(dx^4)/B1;

%number of periods
per=Number_Periods;

%Number of iterations
iter=ceil(per*2*pi/dt);

%increment for visulaization
incr=Data_Increment;

%tolerance
tol=Tolerance;

figure(1),hold on

```

```
figure(2),hold on
figure(3)
```

```
%q is the counter for the total time. It is initialized with the
time step
```

```
%dt
```

```
q=dt;
```

```
%t_end is the final time
```

```
t_end=per*2*pi/mod_freq
```

```
%three counters
```

```
j=1;
```

```
ji=1;
```

```
m1=1;
```

```
tol_min=100;
```

```
while(q<t_end)
```

```
%-----
```

```
%calculate derivative
```

```
du_dxxxx(1)=Fourth_order_CenLeft([u(1) u(2) u(3) u(4) u(5)],dx);
```

```
du_dxxxx(2:n-1)=Fourth_order_Central(u,dx,n+2);
```

```
du_dxxxx(end+1)=Fourth_order_CenRight([u(end-4) u(end-3) u(end-2) u(end-1) u(end)],dx);
```

```

    %pause

for i=1:n+2

    if (i==1)
        u_new(i)=0;
        v_new(i)=0;
    elseif (i==n+2)
        %      u_new(i)=s_factor*(((d(1)/d(4))*(e(3)/e(1)))-(d(3)/d(4)))*u
        (end-1)+...
        %      s_factor*(((d(1)/d(4))*(e(2)/e(1)))-(d(2)/d(4)))*u(end-2);
    elseif (i > 1 && i < n+2)
        v_new(i)=v(i)+(dt/3)*(-B1*du_dxxxx(i-1)-B2*v(i)-F_g+F_e*(1+
            sin(mod_freq*q/3))^2);
        u_new(i)=u(i)+(dt/3)*v(i);
    end

end

end

%boundary conditions
u_new(n+2)=s_factor*(((d(1)/d(4))*(e(3)/e(1)))-(d(3)/d(4)))*u_new(
    end-1)+...
    s_factor*(((d(1)/d(4))*(e(2)/e(1)))-(d(2)/d(4)))*u_new(end-2);
u_new(2)=-(c(1)*u_new(1)/c(2))-(c(3)*u_new(3)/c(2))-(c(4)*u_new(4)/c
    (2));

```

```

%-----

%calculate derivative
du_dxxxx_new(1)=Fourth_order_CenLeft([u_new(1) u_new(2) u_new(3)
    u_new(4) u_new(5)],dx);
du_dxxxx_new(2:n-1)=Fourth_order_Central(u_new,dx,n+2);
du_dxxxx_new(end+1)=Fourth_order_CenRight([u_new(end-4) u_new(
    end-3) u_new(end-2) u_new(end-1) u_new(end)],dx);

%pause

for i=1:n+2

    if(i==1)
        u_new2(i)=0;
        v_new2(i)=0;
    elseif(i==n+2)
        %      u_new2(i)=s_factor*(((d(1)/d(4))*e(3)/e(1))-d(3)/d(4))*
        %      u_new(end-1)+...
        %      s_factor*(((d(1)/d(4))*e(2)/e(1))-d(2)/d(4))*u_new(end-2);
    elseif(i > 1 && i < n+2)
        v_new2(i)=v(i)+(dt/6)*((-B1*du_dxxxx_new(i-1)-B2*v_new(i)-
            F_g+F_e*(1+sin(mod_freq*q/3))^2)+...
            (-B1*du_dxxxx(i-1)-B2*v(i)-F_g+F_e*(1+sin(mod_freq*q/3))
            ^2));
        u_new2(i)=u(i)+(dt/6)*(v_new(i)+v(i));
    end
end

```

end

end

%boundary conditions

```
u_new2(n+2)=s_factor*((d(1)/d(4))*(e(3)/e(1))-(d(3)/d(4)))*u_new2(  
    end-1)+...
```

```
    s_factor*((d(1)/d(4))*(e(2)/e(1))-(d(2)/d(4)))*u_new2(end-2);  
u_new2(2)=-(c(1)*u_new2(1)/c(2))-(c(3)*u_new2(3)/c(2))-(c(4)*u_new2(  
    (4)/c(2));
```

*%*_____

%calculate derivative

```
du_dxxxx_new2(1)=Fourth_order_CenLeft([u_new2(1) u_new2(2)  
    u_new2(3) u_new2(4) ...  
    u_new2(5)],dx);
```

```
du_dxxxx_new2(2:n-1)=Fourth_order_Central(u_new2,dx,n+2);
```

```
du_dxxxx_new2(end+1)=Fourth_order_CenRight([u_new2(end-4) u_new2(  
    (end-3) u_new2(end-2) u_new2(end-1) u_new2(end)],dx);
```

%pause

for i=1:n+2

```

if (i==1)
u_new3(i)=0;
v_new3(i)=0;
elseif (i==n+2)
elseif (i > 1 && i < n+2)
    v_new3(i)=v(i)+(dt/8)*((-B1*du_dxxxx(i-1)-B2*v(i)-F_g+F_e
        *(1+sin(mod_freq*q/2))^2)+...
        3.*(-B1*du_dxxxx_new2(i-1)-B2*v_new2(i)-F_g+F_e*(1+sin(
            mod_freq*q/2))^2));
    u_new3(i)=u(i)+(dt/8)*(v(i)+3.*v_new2(i));
end

end

%boundary conditions
u_new3(n+2)=s_factor*(((d(1)/d(4))*(e(3)/e(1)))-(d(3)/d(4)))*u_new3(
end-1)+...
    s_factor*(((d(1)/d(4))*(e(2)/e(1)))-(d(2)/d(4)))*u_new3(end-2);
u_new3(2)=-(c(1)*u_new3(1)/c(2))-(c(3)*u_new3(3)/c(2))-(c(4)*u_new3
(4)/c(2));

%_____

%calculate derivative
du_dxxxx_new3(1)=Fourth_order_CenLeft([u_new3(1) u_new3(2)

```

```

    u_new3(3) ...
    u_new3(4) u_new3(5) ], dx);
du_dxxxx_new3(2:n-1)=Fourth_order_Central(u_new3, dx, n+2);
du_dxxxx_new3(end+1)=Fourth_order_CenRight([u_new3(end-4) u_new3
    (end-3) u_new3(end-2) u_new3(end-1) u_new3(end)], dx);

%pause

for i=1:n+2

    if(i==1)
    u_new4(i)=0;
    v_new4(i)=0;
    elseif(i==n+2)
%        u_new4(i)=s_factor*(((d(1)/d(4))*e(3)/e(1))-d(3)/d(4))*
u_new3(end-1)+...
%        s_factor*(((d(1)/d(4))*e(2)/e(1))-d(2)/d(4))*u_new3(end-2);
    elseif(i > 1 && i < n+2)
        v_new4(i)=v(i)+(dt/2)*((-B1*du_dxxxx(i-1)-B2*v(i)-F_g+F_e
            *(1+sin(mod_freq*q))^2) - ...
            3.*(-B1*du_dxxxx_new2(i-1)-B2*v_new2(i)-F_g+F_e*(1+sin(
                mod_freq*q))^2) + ...
            4.*(-B1*du_dxxxx_new3(i-1)-B2*v_new3(i)-F_g+F_e*(1+sin(
                mod_freq*q))^2));
        u_new4(i)=u(i)+(dt/2)*(v(i)-3.*v_new2(i)+4.*v_new3(i));
    end

```

end

%boundary conditions

```
u_new4(n+2)=s_factor*(((d(1)/d(4))*e(3)/e(1))-d(3)/d(4))*u_new4(  
    end-1)+...
```

```
    s_factor*(((d(1)/d(4))*e(2)/e(1))-d(2)/d(4))*u_new4(end-2);
```

```
u_new4(2)=-(c(1)*u_new4(1)/c(2))-c(3)*u_new4(3)/c(2))-c(4)*u_new4  
    (4)/c(2));
```

*%*_____

%calculate derivative

```
du_dxxxx_new4(1)=Fourth_order_CenLeft([u_new4(1) u_new4(2)
```

```
    u_new4(3) ...
```

```
    u_new4(4) u_new4(5)],dx);
```

```
du_dxxxx_new4(2:n-1)=Fourth_order_Central(u_new4,dx,n+2);
```

```
du_dxxxx_new4(end+1)=Fourth_order_CenRight([u_new4(end-4) u_new4  
    (end-3) u_new4(end-2) u_new4(end-1) u_new4(end)],dx);
```

%pause

for i=1:n+2

```
    if (i==1)
```

```
        u_new5(i)=0;
```

```

v_new5(i)=0;
elseif(i==n+2)
%       u_new5(i)=s_factor*(((d(1)/d(4))*e(3)/e(1))-d(3)/d(4))*
u_new4(end-1)+...
%       s_factor*(((d(1)/d(4))*e(2)/e(1))-d(2)/d(4))*u_new4(end-2);
elseif(i > 1 && i < n+2)
    v_new5(i)=v(i)+(dt/6)*((-B1*du_dxxxx(i-1)-B2*v(i)-F_g+F_e
        *(1+sin(mod_freq*q))^2)+...
        4.*(-B1*du_dxxxx_new3(i-1)-B2*v_new3(i)-F_g+F_e*(1+sin(
            mod_freq*q))^2)+...
        (-B1*du_dxxxx_new4(i-1)-B2*v_new4(i)-F_g+F_e*(1+sin(
            mod_freq*q))^2));
    u_new5(i)=u(i)+(dt/6)*(v(i)+4.*v_new3(i)+v_new4(i));
end

end

%boundary conditions
u_new5(n+2)=s_factor*(((d(1)/d(4))*e(3)/e(1))-d(3)/d(4))*u_new5
    (end-1)+...
    s_factor*(((d(1)/d(4))*e(2)/e(1))-d(2)/d(4))*u_new5(end-2);
u_new5(2)=-(c(1)*u_new5(1)/c(2))-c(3)*u_new5(3)/c(2))-c(4)*u_new5
    (4)/c(2));

%_____

```

```

err_u(j)=sqrt(sum((u_new5-u_new4).^2));
err_v(j)=sqrt(sum((v_new5-v_new4).^2));

err_max(j)=max([err_u(j) err_v(j)]);

if(err_max(j) >= tol)
dt=dt/2;
u=u;
v=v;
j=j+1;

elseif(err_max(j) <= tol/tol_min)

if(ji==incr*(m1-1)+1)
figure(1),plot(u_new5(end),v_new5(end),'ks')
xlabel('displacement'),ylabel('velocity')
figure(2),plot(q,u_new5(end),'ks')
xlabel('time'),ylabel('displacement')
figure(3),plot(x,u_new5),axis([0.0 1.0 -200 1])
xlabel('position'),ylabel('displacement')
pause(0.1)
pos_out(m1)=u_new5(end);
vel_out(m1)=v_new5(end);
m1=m1+1;

```

end

```
q=q+dt;  
dt=2*dt;  
j=j+1;  
ji=ji+1;  
u=u_new5;  
v=v_new5;
```

elseif(err_max(j) > tol/tol_min && err_max(j) < tol)

```
if (ji==incr*(m1-1)+1)  
    figure (1), plot (u_new5(end), v_new5(end), 'ks')  
    xlabel ('displacement'), ylabel ('velocity')  
    figure (2), plot (q, u_new5(end), 'ks')  
    xlabel ('time'), ylabel ('displacement')  
    figure (3), plot (x, u_new5), axis ([0.0 1.0 -200 1])  
    xlabel ('position'), ylabel ('displacement')  
    pause (0.1)  
    pos_out(m1)=u_new5(end);  
    vel_out(m1)=v_new5(end);  
    m1=m1+1;
```

end

```
q=q+dt;  
j=j+1;  
ji=ji+1;
```

```
u=u_new5;  
v=v_new5;
```

```
end
```

```
clear du_dxxxx  
clear du_dxxxx_new  
clear du_dxxxx_new2  
clear du_dxxxx_new3  
clear du_dxxxx_new4
```

```
end
```

```
save(pos_data_out_1 , 'pos_out' , 'vel_out' ) %Change the *1* to whatever  
the frequency for this data set is!
```

```
%_____
```

```
function u_out=Fourth_order_CenLeft(u,dx)
```

```
[c,T]=TT([-1 0 1 2 3],4);
```

```
u_out=((1/dx)^4) .* (c(1)*u(1)+c(2)*u(2)+c(3)*u(3)+c(4)*u(4)+c(5)*u(5)  
);
```

```
%_____
```

```

function u_out=Fourth_order_CenRight(u,dx)

[c,T]=TT([-3 -2 -1 0 1],4);

u_out=((1/dx)^4).* (c(1)*u(1)+c(2)*u(2)+c(3)*u(3)+c(4)*u(4)+c(5)*u(5)
    );

%-----

function u_out=Fourth_order_Central(u,dx,n)

m=1;

[c,T]=TT([-2 -1 0 1 2],4);

for i=3:n-2
    u_out(m)=((1/dx)^4).* (c(1)*u(i-2)+c(2)*u(i-1)+c(3)*u(i)+c(4)*u(i
        +1)+c(5)*u(i+2));
    m=m+1;
end

%-----

function [c,T]=TT(x,order)

```

```

% Determine the coefficients to a finite differencing scheme
% ie. find the coeffs [c1,c2,c3] that are appropriate for the 2
    nd order
%     cent. diff. approx. to the first derivative :

%  $(du/dx)[j] = 1/dx*(c1*u[j-1] + c2*u[j] + c3*u[j+1]) + error$ 
    terms

% Inputs:
%     x - vector containing relative distances to sampling
    points
%     ie. for example above would be  $x=[-1,0,1]$ 
%     ie. 5 terms full forward:  $x = [0,1,2,3,4]$ 
%     ie. 5 terms central :      $x = [-2,-1,0,1,2]$ 
%
%     order - order of the derivative to approximate

% Outputs:
%     c - the coefficients you're looking for!
%     T optional output matrix showing the Taylor Table
    coefficients

%% The code:
N=numel(x); %number of unknowns
T=zeros(N,N);
for j=1:N % do for each x
    for n=0:N-1 % Do for each coeff of the Taylor expansion

```

```
T(j ,n+1)=-1/factorial(n)*x(j)^n;  
end  
end  
  
% Vector holding place of the derivative  
d=zeros(N,1);  
d(order+1)=-1;  
  
% Calculate the coefficients  
c=T'\d;
```